The blue supergiant MN18 and its bipolar circumstellar nebula*

V. V. Gvaramadze,[1,2,3]† A. Y. Kniazev,[1,4,5] J. M. Bestenlehner,[6,7] J. Bodensteiner,[8,9]
N. Langer,[6] J. Greiner,[9] E. K. Grebel,[10] L. N. Berdnikov[1,3,11] and Y. Beletsky[12]

[1]*Sternberg Astronomical Institute, Lomonosov Moscow State University, Universitetskij Pr. 13, Moscow 119992, Russia*
[2]*Space Research Institute, Russian Academy of Sciences, Profsoyuznaya 84/32, 117997 Moscow, Russia*
[3]*Isaac Newton Institute of Chile, Moscow Branch, Universitetskij Pr. 13, Moscow 119992, Russia*
[4]*South African Astronomical Observatory, PO Box 9, 7935 Observatory, Cape Town, South Africa*
[5]*Southern African Large Telescope Foundation, PO Box 9, 7935 Observatory, Cape Town, South Africa*
[6]*Argelander-Institut für Astronomie der Universität Bonn, Auf dem Hügel 71, 53121, Bonn, Germany*
[7]*Max-Planck Institute for Astronomy, D-69117, Heidelberg, Germany*
[8]*Technische Universität München, Physik Dept., James-Franck-Str., 85748 Garching, Germany*
[9]*Max-Planck-Institut für extraterrestrische Physik, Giessenbachstraße 1, D-85748, Garching, Germany*
[10]*Astronomisches Rechen-Institut, Zentrum für Astronomie der Universität Heidelberg, Mönchhofstr. 12–14, 69120 Heidelberg, Germany*
[11]*Astronomy and Astrophysics Research division, Entoto Observatory and Research Center, P.O.Box 8412, Addis Ababa, Ethiopia*
[12]*Las Campanas Observatory, Carnegie Institution of Washington, Colina el Pino, Casilla 601 La Serena, Chile*

ABSTRACT

We report the results of spectrophotometric observations of the massive star MN18 revealed via discovery of a bipolar nebula around it with the *Spitzer Space Telescope*. Using the optical spectrum obtained with the Southern African Large Telescope, we classify this star as B1 Ia. The evolved status of MN18 is supported by the detection of nitrogen overabundance in the nebula, which implies that it is composed of processed material ejected by the star. We analysed the spectrum of MN18 by using the code CMFGEN, obtaining a stellar effective temperature of $\approx$21 kK. The star is highly reddened, $E(B-V)\approx2$ mag. Adopting an absolute visual magnitude of $M_V=-6.8\pm0.5$ (typical of B1 supergiants), MN18 has a luminosity of $\log L/\,\mathrm{L_\odot}\approx5.42\pm0.30$, a mass-loss rate of $\approx(2.8-4.5)\times10^{-7}\,\mathrm{M_\odot\,yr^{-1}}$, and resides at a distance of $\approx5.6^{+1.5}_{-1.2}$ kpc. We discuss the origin of the nebula around MN18 and compare it with similar nebulae produced by other blue supergiants in the Galaxy (Sher 25, HD 168625, [SBW2007] 1) and the Large Magellanic Cloud (Sk$-69°202$). The nitrogen abundances in these nebulae imply that blue supergiants can produce them from the main sequence stage up to the pre-supernova stage. We also present a K-band spectrum of the candidate luminous blue variable MN56 (encircled by a ring-like nebula) and report the discovery of an OB star at $\approx$17 arcsec from MN18. The possible membership of MN18 and the OB star of the star cluster Lynga 3 is discussed.

Key words: circumstellar matter – stars: emission-line, Be – stars: individual: [GKF2010] MN18, [GKF2010] MN56, [GKF2010] MN109 – supergiants – stars: winds, outflows – open clusters and associations: individual: Lynga 3.

1 INTRODUCTION

Massive stars change their mass-loss rate, and the velocity, symmetry and composition of their copious winds in the course of their evolution. The mass loss along with stellar rotation and magnetic fields, and effects of binarity (various modes of mass transfer between binary components, mergers of the components, common-envelope ejection) result in the formation of different types of circumstellar nebulae, of

which the hourglass-like type is most spectacular. The first and the best known example of such a nebula associated with a massive star is that created by the Large Magellanic Cloud B-type supergiant Sk$-69°202$ – the progenitor of the SN 1987A (Plait et al. 1995; Burrows et al. 1995). Later, a number of Galactic analogs of this nebula were discovered around the already known blue supergiants – the candidate luminous blue variables (cLBVs) Sher 25 (Brandner et al. 1997a), HD 168625 (Smith 2007) and MWC 349A (Gvaramadze & Menten 2012), and the newly identified blue supergiant [SBW2007] 1 (Smith, Bally & Walawender 2007).

There is still no complete understanding on how and in which evolutionary phases massive stars form their circumstellar nebulae. The nebulae can definitely originate during the late and final (pre-supernova) phases, as evidenced by the detection of numerous compact shells of processed material around Wolf-Rayet stars (e.g. Chu, Treffers & Kwitter 1983; Esteban et al. 1992; Dopita et al. 1994; Marston 1995; Stock, Barlow & Wesson 2011) and the three-ring nebula associated with the SN 1987A. Under proper conditions, compact shells could form around red supergiants (Mackey et al. 2014), which unlike the shells around Wolf-Rayet stars could exist until their central stars explode as supernovae. The majority of candidate and bona fide LBVs are also associated with compact circular or bipolar nebulae (Nota et al. 1995; Clark, Larionov & Arkharov 2005; Kniazev, Gvaramadze & Berdnikov 2015) and there is evidence that some of these stars might be the immediate precursors of supernovae (e.g. Kotak & Vink 2006; Groh, Meynet & Ekström 2013; Justham, Podsiadlowski & Vink 2014). On the other hand, the analysis of the heavy element abundances in circumstellar nebulae around several LBVs by Lamers et al. (2001) led them to suggest that these nebulae were created at the end of the main sequence. Similarly, it was argued that enhanced mass loss at the beginning of the blue supergiant phase was responsible for the origin of the bipolar nebula around the cLBV Sher 25 (Smartt et al. 2002; Hendry et al. 2008) and a multi-shell nebula associated with the late O-type supergiant TYC 3159-6-1 (Gvaramadze et al. 2014a). Which of the evolutionary phases are more prone to produce circumstellar nebulae in general and the bipolar ones in particular still needs to be determined. Clarifying this point is important for estimating the production rate of different types of nebulae and for the comprehension of the mechanisms responsible for their origin.

A large number of models have been proposed to explain the formation of bipolar nebulae. The vast majority of them assume that the spherically symmetric stellar wind is collimated by a disk-like (equatorial) circumstellar environment, whose origin and geometry could be attributed to either an asymmetric mass loss during the preceding stellar evolutionary phase (e.g. Blondin & Lundqvist 1993; Martin & Arnett 1995; Frank, Balick & Davidson 1995; Langer, Garía-Segura & Mac Low 1999) or to various binary interaction processes (e.g. Morris 1981; Fabian & Hansen 1979; Mastrodemos & Morris 1999; Morris & Podsiadlowski 2009). In some models, the stellar wind is considered to be intrinsically bipolar, e.g. because of nearly critical stellar rotation (Owocki & Gayley 1997; Maeder & Desjacques 2001; Chita et al. 2008). It is quite likely that several mechanisms for shaping bipolar nebulae could be at work. The detection of new examples of bipolar outflows from massive stars might

be essential for the identification of relevant mechanisms for their origin as well as for a better understanding at which stellar evolutionary phase(s) these mechanisms start to operate.

In our search for compact mid-infrared nebulae in the archival data of the *Spitzer Space Telescope* (for the motivation and some results of this search, see Gvaramadze et al. 2009, 2010a,b, 2014b; Gvaramadze, Kniazev & Fabrika 2010c, hereafter Paper I), we detected two striking examples of hourglass-like nebulae, which were presented for the first time and named MN13 and MN18[1] in Paper I (see table 1 and figs 3 and 10 there). MN18 and its central star (in the following, we will use the name MN18 only for the star) are the subject of this paper and presented in Section 2. Section 3 describes our spectroscopic and photometric observations of MN18. The spectral classification of MN18 is given in Section 4, where we also determine the fundamental parameters of this star using the radiative transfer code CMFGEN and estimate its luminosity. Spectroscopy of the nebula is discussed in Section 5. In Section 6, we discuss the origin of bipolar nebulae around evolved massive stars and compare the nebula around MN18 with other similar bipolar nebulae. The possible parent cluster of MN18 is discussed in Section 6 as well.

2   MN18 AND ITS BIPOLAR NEBULA

The blue supergiant MN18 is one of many dozens of evolved massive stars revealed through the detection of their circumstellar nebulae with the *Spitzer Space Telescope* (see Table 1 in Paper I). The bipolar nebula around MN18 was discovered in archival 24 μm data obtained with the Multiband Imaging Photometer for *Spitzer* (MIPS; Rieke et al. 2004) within the framework of the 24 and 70 Micron Survey of the Inner Galactic Disk with MIPS (Carey et al. 2009). This nebula appears as two lobes protruding for about 70 arcsec in the northwest and southeast directions from a bright waist centred on MN18. At a distance of d=5.6 kpc (see Section 4), the linear extent of the lobes is $\approx$1.9 pc.

Fig. 1 shows the nebula in three different intensity scales to highlight some details of its structure. The low intensity image of the waist of the nebula revealed two bright spots on each side of MN18 (the star itself is not visible at 24 μm). We interpret these spots as cross-sections of a toroidal equatorial ring around the star visible nearly edge-on. The northwest lobe appears to be opened along the polar axis, while in the southeast lobe one can discern two incomplete ellipse-like filaments oriented plane parallel to the equatorial ring. These filaments are reminiscent of a polar ring associated with the cLBV HD 168625 (see fig. 1d in Smith 2007 and fig. 2n in Paper I), but both are located on the same side of the torus. Assuming rotational symmetry for the nebula, the aspect ratios of the filaments suggest that the nebula is inclined with respect to the plane of sky by $\approx$30°. Correspondingly, the inclination angle of the stellar rotational axis to our line of sight, i, is $\approx$60°. Fig. 1 also shows a bright feature attached

---

[1] In the Set of Identifications, Measurements and Bibliography for Astronomical Data (SIMBAD) data base these shells are named [GKF2010] MN13 and [GKF2010] MN18.
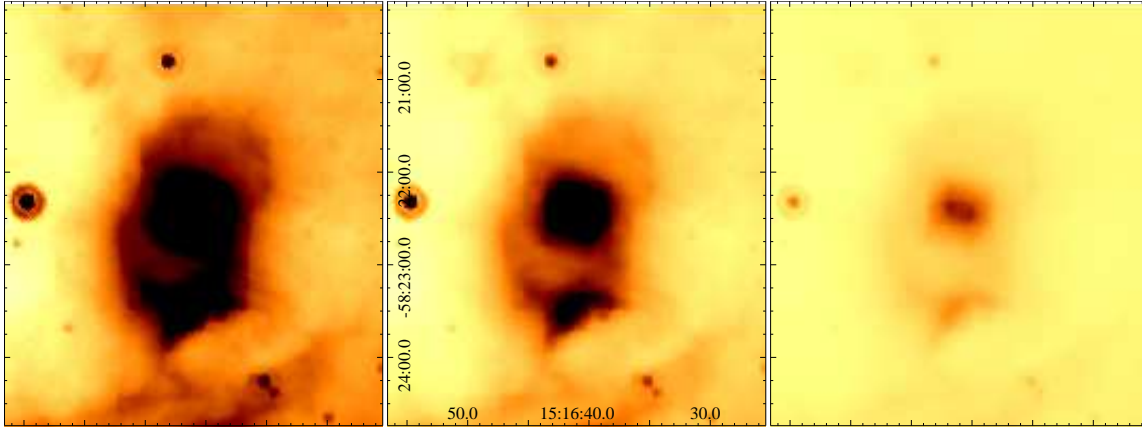
Figure 1. *Spitzer* MIPS 24 μm image of the bipolar nebula around MN18 at three intensity scales, highlighting various details of its structure. The coordinates are in units of RA (J2000) and Dec. (J2000) on the horizontal and vertical scales, respectively. At an adopted distance of 5.6 kpc, 1 arcmin corresponds to ≈1.6 pc.
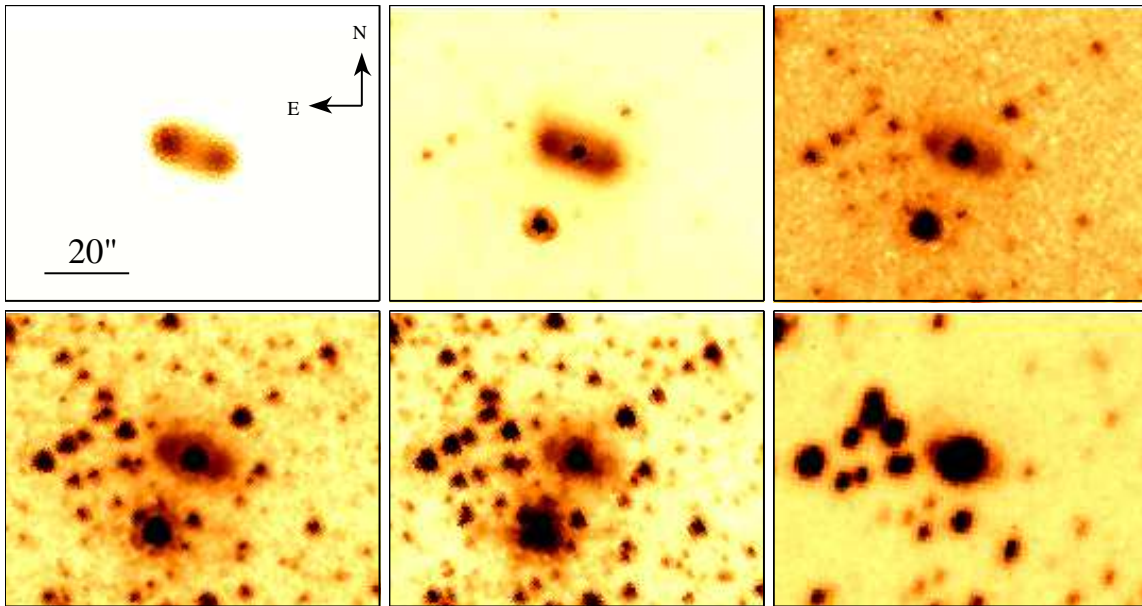

Figure 2. From left to right, and from top to bottom: *Spitzer* MIPS 24 μm, IRAC 8, 5.8, 4.5 and 3.6 μm, and SHS Hα+[N II] images of the equatorial ring around MN18. MN18 and several stars around it were proposed by Lynga (1964a) to be members of the same star cluster (see Section 6.4 for more details).

to the southwestern edge of the southeast lobe. A possible origin of this feature is discussed in Section 6.4.

MN18 and its equatorial ring are clearly visible in all (3.6, 4.5, 5.8 and 8.0 μm) images (see Fig. 2) obtained with the *Spitzer* Infrared Array Camera (IRAC; Fazio et al. 2004) within the Galactic Legacy Infrared Mid-Plane Survey Extraordinaire (GLIMPSE; Benjamin et al. 2003). The northeast half of the ring is ≈20 per cent brighter than the southwest one. The semimajor and semiminor axes of the nebula are ≈11 and 4.5 arcsec, respectively. For d=5.6 kpc, the linear radius of the waist is ≈0.29 pc. The 8 μm image also shows a "horn" at the northeast edge of the equatorial ring, which might correspond to the beginning of the northwest lobe. Similar horns could also be seen in the IRAC images

of the equatorial rings of the cLBVs Sher 25 and MN56 (see, respectively, fig. 2l and fig. 4 in Paper I).

The IRAC images of the waist of the bipolar nebula were presented for the first time by Kwok et al. (2008), who classified it as a planetary nebula (PN) and named PNG 321.0−00.7[2]. Kwok et al. (2008) also noted that PNG 321.0−00.7 has an optical counterpart in the Super-COSMOS H-alpha Survey (SHS; Parker et al. 2005), but

---

[2] Anderson et al. (2012) used mid- and far-infrared colours of PNG 321.0−00.7 to suggest that this object is likely a PN, while Cohen et al. (2011) confused it with another PN candidate from Kwok et al. (2008), PNG 306.4+00.2, and proposed that PNG 321.0−00.7 might be a reflection nebula (see their table 1).

Table 1. Details of MN18.

Spectral type	B1 Ia
RA(J2000)	$15^{\rm h}16^{\rm m}41\overset{\rm s}{.}01$
Dec.(J2000)	$-58°22'26''\!.0$
l	$321°\!.0239$
b	$-0°\!.6992$
B (mag)	15.34 ± 0.01
V (mag)	13.40 ± 0.01
$I_{\rm c}$ (mag)	10.91 ± 0.01
J (mag)	9.22 ± 0.02
H (mag)	8.72 ± 0.02
$K_{\rm s}$ (mag)	8.38 ± 0.02
[3.6] (mag)	8.02 ± 0.04
[4.5] (mag)	7.99 ± 0.06
[5.8] (mag)	7.88 ± 0.05
[8.0] (mag)	8.01 ± 0.14

did not show its image. Fig. 10 in Paper I presented the SHS Hα+[N II] image of the waist for the first time (see also Fig. 2).

In Paper I, we provisionally classified MN18 as an early B supergiant, using a spectrum obtained with the 1.9-m telescope of the South African Astronomical Observatory (SAAO) (see Section 3.1). Our subsequent spectroscopy with the Southern African Large Telescope (SALT) allowed us to refine this classification to B1 Ia (see Section 4.1).

The details of MN18 are summarized in Table 1. The $BVI_{\rm c}$ magnitudes are the mean values derived from our five CCD measurements listed in Table 3. The coordinates and the $JHK_{\rm s}$ photometry are taken from the Two-Micron All Sky Survey (2MASS) All-Sky Catalog of Point Sources (Cutri et al. 2003). The IRAC photometry is from the GLIMPSE Source Catalog (I + II + 3D) (Spitzer Science Center 2009).

MN18 is one of the 25 stars with $V < 15$ mag, which were suggested by Lynga (1964a) to be members of the open star cluster Ly 3, called Lynga 3 in the SIMBAD[3] and WEBDA[4] (Mermilliod 1995) data bases. MN18 has the sequence number 22 in table V of Lynga (1964a), which gives photographic B and V magnitudes of 15.6 and 13.3, respectively, for this star. The relationship between MN18 and Lynga 3 is further discussed in Section 6.4.

3 MN18: OBSERVATIONS

3.1 Spectroscopic observations

The first spectrum of MN18 was obtained with the SAAO 1.9-m telescope on 2009 May 27. The observations were performed with the Cassegrain spectrograph using a slit of 3 arcmin × 1.8 arcsec and grating with 300 lines mm^{-1}. The slit was oriented at a position angle (PA) of PA=80°, measured from north to east. This spectral setup covered a wavelength range of $\approx$4200–8100 Å with a reciprocal dispersion of $\approx$2.3 Å pixel^{-1} and a spectral resolution full width at half-maximum (FWHM) of $\approx$7 Å. Three exposures of 900 s were taken with a seeing of $\approx$2 arcsec.

The obtained spectrum (see fig. 9 of Paper I) revealed numerous H and He I lines in absorption and prominent nebular emissions – the Hα line flanked by the [N II] $\lambda\lambda$6548, 6584 lines. Unfortunately, the stellar and the nebular spectra were too weak to allow us to obtain a reliable spectral classification of MN18 and to derive any useful information on the nebula.

To classify MN18 and to study the nebula, we obtained a new spectrum (we call it low-resolution hereafter) with the SALT (Buckley, Swart & Meiring 2006; O'Donoghue et al. 2006) on 2012 March 2, using the Robert Stobie Spectrograph (RSS; Burgh et al. 2003; Kobulnicky et al. 2003) in the long-slit mode with a slit of 8 arcmin×1.5 arcsec. The slit was oriented along the major axis of the optical nebula, i.e. at PA=72°. The PG900 grating was used to cover the spectral range of 4200−7300 Å with a final reciprocal dispersion of 0.97 Å pixel^{-1} (FWHM≈5.50 Å). A 300 s spectrum was taken with 2×2 binning. The RSS uses a mosaic of three 2048×4096 CCDs and the final spatial scale for this observation was $0''\!.25$ pix^{-1}. The seeing during the observation was ≈1.3 arcsec. A Xe lamp arc spectrum was taken immediately after the science frame. A spectrophotometric standard star was observed during twilight time for relative flux calibration.

To study the velocity distribution along the optical nebula, two additional higher resolution long-slit spectra (high-resolution spectra hereafter) were obtained with the RSS using the grating PG2300 on 2013 April 26 and 27. A slit with a width of 1.25 arcsec was used in both observations with the same PA as earlier. A spectral range of 6035−6900 Å was covered with a final reciprocal dispersion of 0.27 Å pixel^{-1} and a FWHM spectral resolution of 1.33 Å. One 900 s spectrum was taken with a 2×4 binning each night with a spatial scale of $0''\!.51$ pix^{-1} along the slit. The seeing during the observations was 1.5 arcsec. A Ne lamp arc spectrum and a set of Quartz Tungsten Halogen flats were taken immediately after the science frames, and a spectrophotometric standard star was observed during twilight time for relative flux calibration.

The primary reduction of the SALT data was carried out with the SALT science pipeline (Crawford et al. 2010). After that, the bias and gain corrected and mosaiced long-slit data were reduced in the way described in Kniazev et al. (2008). Absolute flux calibration is not feasible with SALT because the unfilled entrance pupil of the telescope moves during the observation. However, a relative flux correction to recover the spectral shape was done using the observed spectrophotometric standard.

For spectral modelling and to derive the rotational velocity, we obtained high-resolution spectra of MN18 with the 2.2-m Max Planck Gesellschaft telescope at La Silla (European Southern Observatory; ESO). The data were taken on 2014 March 8 and 9 with the Fibre-fed Extended Range Optical Spectrograph (FEROS; Kaufer et al. 1999) – a high-resolution Échelle spectrograph with an aperture of 2 arcsec, which provides a resolution of 0.038 Å pixel^{-1}. A 2048×4096 CCD was used to record 39 orders covering the spectral range of 3500–9500 Å. Nine 1800 s exposures were obtained, of which three were taken during the first night. The seeing during the observation was below 1.5 arcsec in both nights. Wavelength calibration frames were obtained with ThArNe lamps. A spectrophotometric standard star was observed di-

Table 2. Journal of the observations.

Spectrograph	Date	Exposure (min)	Spectral scale (Å pixel^{-1})	Spatial scale (arcsec pixel^{-1})	Slit (arcsec)	Spectral range (Å)
Cassegrain (SAAO 1.9-m)	2009 May 27[a]	3×15	2.3	1.4	1.8×180	4200−8100
RSS (SALT)	2012 March 2	5	0.97	0.25	1.5×480	4200−7300
RSS (SALT)	2013 April 26	15	0.27	0.51	1.25×480	6035−6900
RSS (SALT)	2013 April 27	15	0.27	0.51	1.25×480	3500−9500
FEROS (MPG 2.2-m)	2014 March 8	3×30	0.038	−	−	3815−5440
FEROS (MPG 2.2-m)	2014 March 9	6×30	0.038	−	−	3815−5440

Note. [a]Presented for the first time in Paper I.

rectly before the target observation in order to perform a flux calibration.

The reduction of the FEROS data, including flatfield correction, bias and background subtraction, order tracing, wavelength and flux calibration, was performed manually with the FEROS Data Reduction Software based on ESO-MIDAS.

The log of our spectroscopic observations is listed in Table 2.

3.2 Photometry

To detect possible photometric variability of MN18, we determined its B, V and I_c magnitudes on CCD frames obtained with the 76-cm telescope of the SAAO during our five observing runs in 2009–2014. We used an SBIG ST-10XME CCD camera equipped with BVI_c filters of the Kron-Cousins system (see e.g. Berdnikov et al. 2012). We also calibrated the 1.9-m telescope spectrum and synthesized its V magnitude in the way described in Kniazev et al. (2005). Additionally, the V magnitude of MN18 was measured on V band images taken before each SALT spectroscopic observation. For this we used secondary photometric standards calibrated with the 76-cm telescope data. Using the same data, we also re-calibrated the photographic B and V magnitudes of MN18 from Lynga (1964a). The resulting photometry is presented in Table 3.

From Table 3 it follows that MN18 did not experience major changes in its brightness: during the last five years its B, V and I_c magnitudes changed by $\lesssim 0.1$ mag, while its $B - V$ and $B - I_c$ colours remained almost constant with mean values of 1.94±0.01 and 4.43±0.01 mag, respectively.

4 MN18: SPECTRAL ANALYSIS AND STELLAR PARAMETERS

4.1 Classification of MN18 and changes in the Hα line

The normalized low- and high-resolution SALT spectra of MN18 are presented in Fig. 3, with the principal lines and most prominent diffuse interstellar bands (DIBs) indicated. All wavelengths are given in air. Equivalent widths (EWs), FWHMs and heliocentric radial velocities (RVs) of the main lines in the low-resolution spectrum (measured applying the MIDAS programs; see Kniazev et al. 2004 for details) are summarized in Table 4.

Fig. 3 shows that the spectrum of MN18 is dominated by

Table 3. Photometry of MN 18.

Date	B	V	I_c
1963 April 4–17[a]	15.46±0.25	13.28±0.21	−
2009 May 27[b]	−	13.35±0.03	−
2010 January 22[c]	15.36±0.01	13.42±0.01	10.94±0.01
2012 March 2[d]	−	13.33±0.04	−
2012 May 6[c]	15.30±0.01	13.36±0.01	10.87±0.01
2013 January 13[c]	15.34±0.01	13.41±0.01	10.90±0.01
2013 April 26[d]	−	13.44±0.04	−
2014 January 18[c]	15.33±0.02	13.43±0.01	10.92±0.01
2014 April 8[c]	15.38±0.02	13.41±0.02	10.94±0.02

Note: [a]Lynga (1964a); [b]1.9-m telescope; [c]76-cm telescope; [d]SALT.

Table 4. EWs, FWHMs and RVs of main lines in the low-resolution spectrum of MN18.

λ_0(Å) Ion	EW(λ) (Å)	FWHM(λ) (Å)	RV (km s^{-1})
4340 Hγ	1.61±0.04	8.68±0.41	-55±9
4388 He I	0.26±0.02	8.46±0.67	-22±8
4471 He I	0.94±0.04	7.03±0.36	-51±8
4481 Mg II	0.18±0.02	5.33±0.90	2±8
4553 Si III	0.56±0.02	6.34±0.23	-63±8
4713 He I	0.18±0.01	4.85±0.21	-11±8
4861 Hβ	1.61±0.05	9.19±0.31	-48±8
4922 He I	0.59±0.01	6.40±0.17	-37±7
5045 N II	0.31±0.01	8.85±0.39	-44±7
5667 N II	0.53±0.02	8.13±0.18	-68±6
5680 N II	0.82±0.02	8.13±0.18	-104±6
5740 Si III	0.67±0.01	7.30±0.17	-34±6
5876 He I	0.90±0.02	6.91±0.17	-78±6
6563 Hα[a]	0.20±0.01	6.70±0.21	−221±5
6678 He I	1.15±0.02	6.51±0.15	-69±6
7065 He I	1.13±0.04	9.41±0.41	-90±5

Note: [a]The RV of this line is noticeably affected by the P Cygni absorption.

absorption lines of H and He I. In the high-resolution spectrum the Hα line is in emission and shows a P Cygni profile. Other prominent absorption lines are those of N II λλ5001-5, 5045, 5667, 5680, 6380, 6482, O II λλ4350, 4415-17, 4640-50, 6721, Mg I λ4471, Si III λλ4553-68-75, 4650 5740, and C II λλ6578, 6583. No He II lines are present in the spectrum,
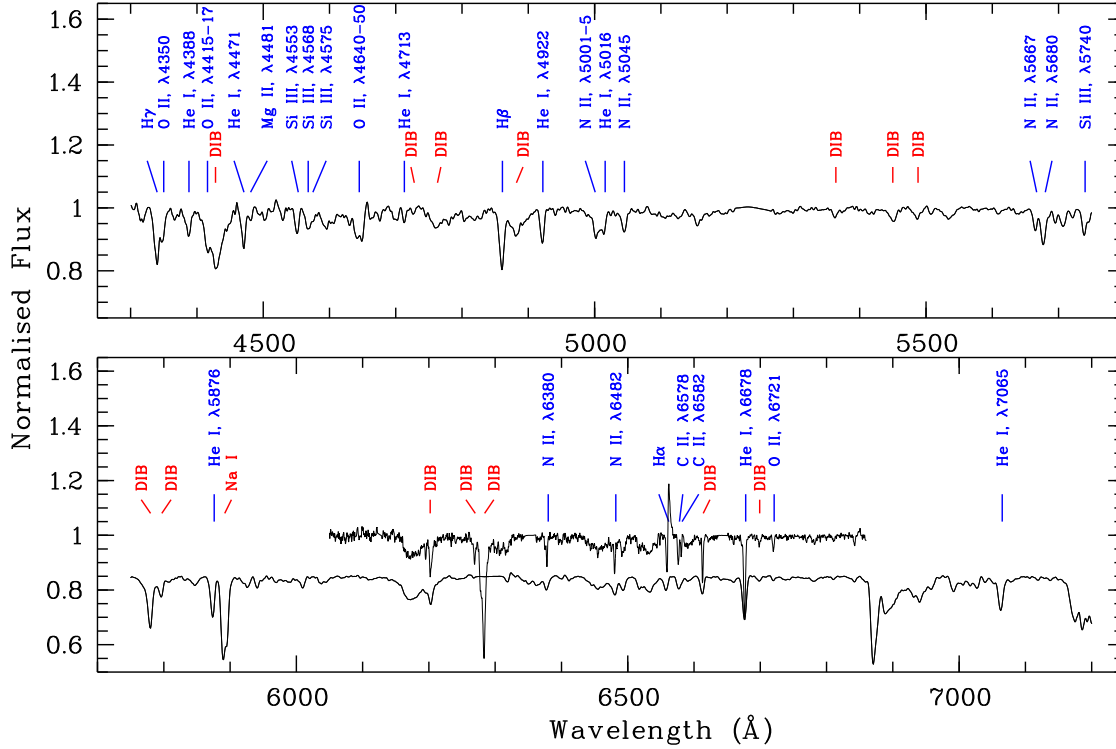
Figure 3. Normalized low-resolution spectrum of MN18 obtained with the SALT on 2012 March 2 with the principal lines and most prominent DIBs indicated. The lower panel also shows the high-resolution spectrum obtained with the SALT on 2013 April 27.

which implies that MN18 is of spectral type of B1 or later (Walborn & Fitzpatrick 1990).

Using the spectral atlas of OB stars by Walborn & Fitzpatrick (1990), we classify MN18 as a B1 Ia star. The Ia luminosity class also follows from the measured EW(Hγ) of 1.61 ± 0.04 Å and the calibrations of Balona & Crampton (1974; see their table V).

The high interstellar extinction towards MN18 (see Sections 4.2 and 5.1) is manifested in numerous DIBs, the most prominent of which are at 4429, 4762, 4881, 5780, 5797, 6203, 6269, 6283 and 6614 Å.

Inspection of the spectra of MN18 obtained in 2009–2014 did not reveal significant changes in their appearance, except for the variability of the Hα line. It was in emission in 2009 and 2013, in absorption in 2012, and in transition between these two states in 2014, with the line centre in absorption and the line wings in emission. Comparison of the SALT high-resolution spectra obtained during two consecutive nights in 2013 shows that the Hα line (and the C II $\lambda\lambda$6578, 6583 doublet as well) changes its shape on a daily time-scale (see Fig. 4), which is typical of early-type supergiants (e.g. Morel et al. 2004; Martins et al. 2015). This variability introduces an ambiguity in mass-loss estimates based on synthesizing the Hα line with model stellar atmosphere codes (see Section 4.2).

Using the 1.9-m telescope and SALT spectra, we searched for shifts in RV as a result of possible binarity of MN18 and found that all measurements agree with each other within their error margins.
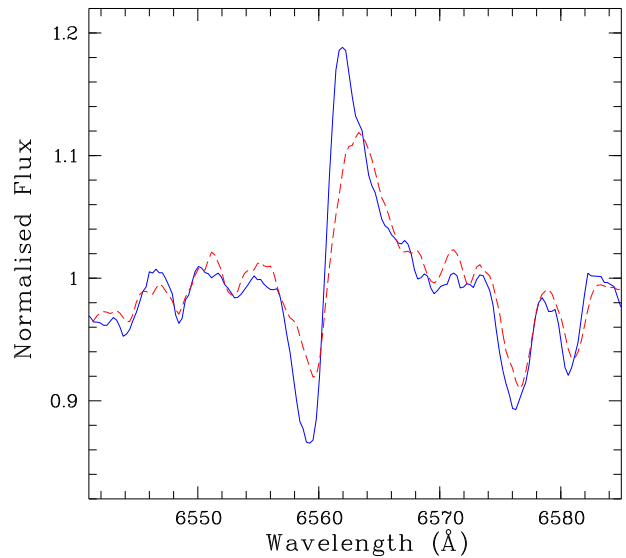

Figure 4. Daily time-scale line profile variability in Hα and the C II $\lambda\lambda$6578, 6583 doublet: 2013 April 26 (solid line) and 2013 April 27 (dashed line).
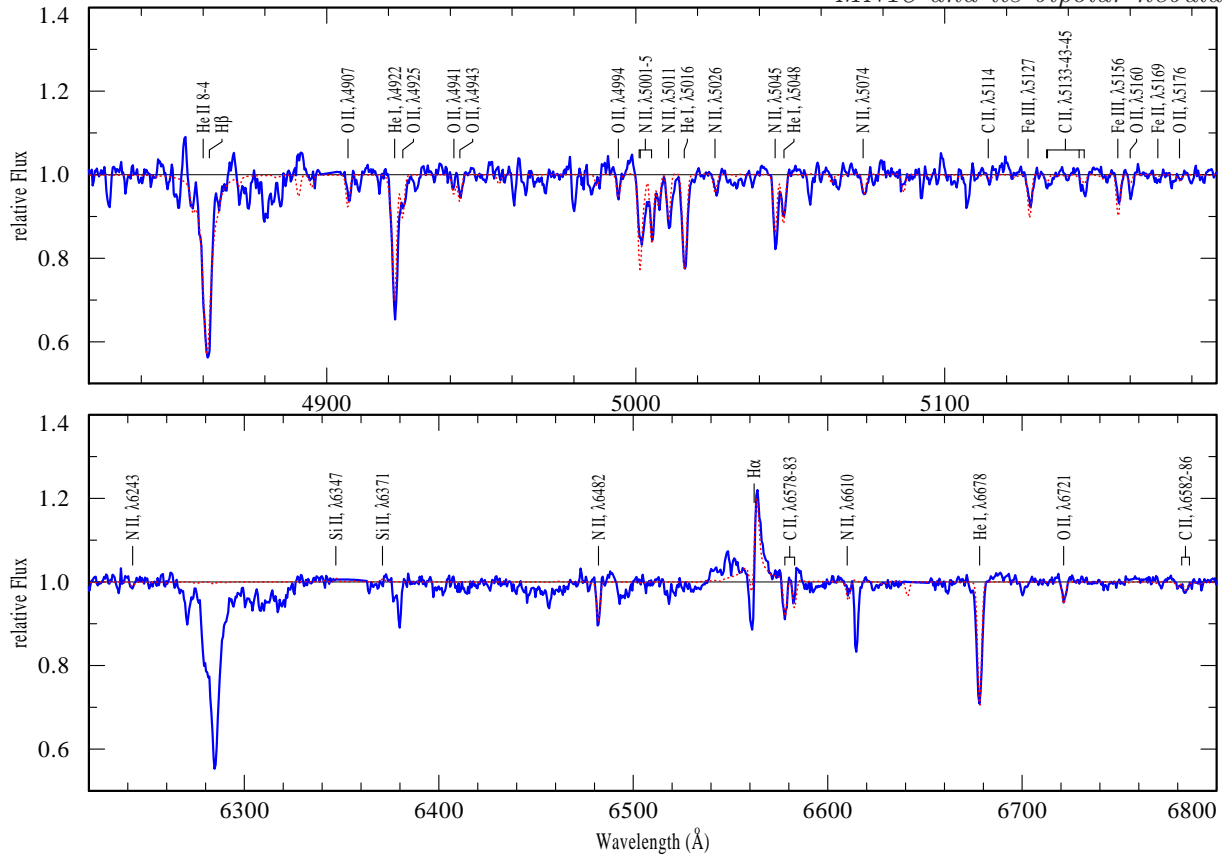
Figure 5. Parts of the normalized FEROS (upper panel) and high resolution SALT (bottom panel) spectra of MN18 (shown by blue solid lines), compared with the best-fitting model spectrum (red dotted line) with the parameters as given in Table 5.
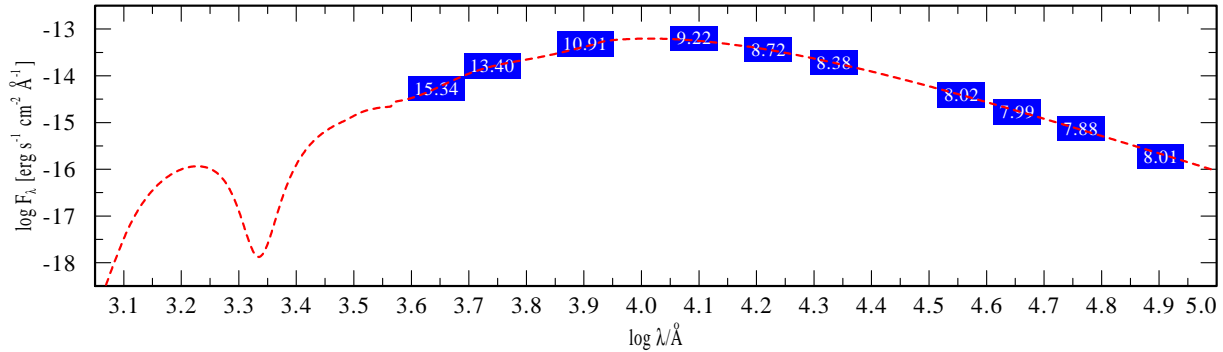

Figure 6. Observed flux distribution of MN18 in absolute units, based on the photometric measurements (blue rectangles) compiled in Table 1, compared to the emergent flux of the reddened model spectrum (red dashed line) with the parameters as given in Table 5.

4.2 Spectral modelling

For the spectral analysis we used spectra from three epochs: the low- and high-resolution SALT spectra taken on 2012 March 2 and 2013 April 27, respectively, and the echelle FEROS spectrum taken on 2014 March 9. Our analysis is based on synthetic spectra computed with the non-LTE stellar atmosphere code CMFGEN (Hillier & Miller 1998). The following model atoms and ions were taken into account: H I, He I-II, C I-IV, N III-V, O I-V, Mg II, Al II, Si II-IV and Fe I-V. Because we are mainly interested in the evolutionary status of MN18, we varied only the abundances of He, C, N and O, while the abundances of other metals are set at solar values

(taken from Asplund et al. 2005). Since our spectra did not cover the UV resonance lines, we cannot resolve the degeneracy between the wind velocity law, β, and a wind volume filling factor of optically thin (micro) clumps, f_v. Similar line profiles for Hα can be achieved by varying β and/or f_v. Based on our model computations, β ranges between 1.5 and 2.5, and f_v between 0.25 and 1.0. In order to estimate the error bars in the effective temperature, $T_{\rm eff}$, mass-loss rate, $\dot{M}$, and surface gravity, $\log g$, we computed a grid of models around the preferred values. The best-fitting model is shown in Fig. 5.

$T_{\rm eff}$ is based on the ratio of the Fe II and III lines and the

intensity of the He I, N II and Si II ones, and is 21.1±1.0 kK. We employed Hβ to determine $\log g$=2.75±0.20. The uncertainty of $\log g$ is rather large as a result of low signal to noise ratio in the FEROS and low resolution in the SALT spectra. The terminal velocity, v_∞, is difficult to constrain due to the weak emission of Hα. No other suitable lines are available in the covered wavelength range. Therefore, the uncertainty is large and we estimate v_∞ of $\approx$1400±500 km s^{-1}. For comparison, we used the relation between v_∞ and the photospheric escape velocity, v_{esc}, from Lamers, Snow & Lindholm (1995), which for T_{eff} = 21.1 kK, $\log g$=2.75 and the bolometric luminosity of $\log(L/L_\odot)$=5.42 (see below) gives v_∞/v_{esc} = 2.6 and v_∞=1370±250 km s^{-1}.

The mass-loss rates for the three epochs were derived from Hα. Over these epochs the profile of Hα changed and, correspondingly, $\dot{M}$ as well. The obtained values for the individual epochs with $\log(L/L_\odot)$=5.42, v_∞=1400 km s^{-1}, β=2.0 and f_v=1.0 are $\log(\dot{M}/M_\odot\,yr^{-1})$=−6.38±0.25[5] (2012 March 2), −6.17±0.25 (2013 April 27), and −6.37±0.25 (2014 March 9). We observe a variation of $\dot{M}$ by a factor of $\approx$1.6. The errors in $\dot{M}$ account for the uncertainties in $\log(L/L_\odot)$, v_∞, β-parameter and micro-clumping. Petrov et al. (2014) found that the optical depth of the Hα line below the bi-stability jump ($T_{eff}\approx$22.5 kK) increases with decreasing T_{eff}. Correspondingly, the profile of this line becomes sensitive to macro-clumping and the derived $\dot{M}$ could be underestimated. However, the effective temperature of MN18 is close to that of the bi-stability jump, while the v_∞/v_{esc} ratio of 2.6 suggests that MN18 has wind properties expected for a star on the hot side of this jump. Therefore, it appears likely that the influence of the macro-clumping on the mass loss rate of MN18 is small, i.e., negligible in comparison to the overall uncertainties.

The CNO abundances are based on the ratio of the C, N and O spectral lines. Table 5 shows that C is reduced by a factor of $\approx$3.5 and N is enriched by $\approx$4 times due to the CNO cycle. The abundance of O is still close to its initial value within the error margins. At the given wavelength range the H and He lines are insensitive to changes in the He abundance, so that the He mass fraction could not be derived.

To estimate the reddening towards MN18, we match the model spectral energy distribution (SED) with the observed one in the B, V and K_s bands (see Table 1). We extracted intrinsic $B − V$ and $V − K_s$ colours from the model flux by applying approximate filter functions[6] and match the resulting values of the colour excesses $E(B − V)$ and $E(V − K_s)$ as described by Bestenlehner et al. (2011) to determine the total-to-selective absorption ratio R_V and V band extinction A_V. We derive $\log(L/L_\odot)$=5.42±0.2 adopting the absolute visual magnitude of M_V=−6.8±0.5 typical of B Ia supergiants (Crowther et al. 2006). Accounting for the uncertainty in T_{eff} and photometric errors, the uncertainty in $\log(L/L_\odot)$ sums up to ±0.3 dex. Even though we find a variability in Hα, the temperature and bolometric cor-

Table 5. Stellar and extinction parameters for MN18.

T_{eff} (kK)	21.1±1.0
$\log(L/L_\odot)$	5.42±0.30
R_* (R$_\odot$)	$38.5^{+18.5}_{-12.7}$
$\log g$	2.75±0.20
$\log(\dot{M}/M_\odot\,yr^{-1})$[a]	−6.38±0.25
$\log(\dot{M}/M_\odot\,yr^{-1})$[b]	−6.17±0.25
$\log(\dot{M}/M_\odot\,yr^{-1})$[c]	−6.37±0.25
β	1.5 to 2.5
f_v	0.25 to 1.0
v_∞ (km s^{-1})	1400±500
v_{eq} (km s^{-1})	104±7
C (mass fraction)	6.5±2.5×10^{-4}
N (mass fraction)	$2.4^{+2.1}_{-1.3} \times 10^{-3}$
O (mass fraction)	$5.4^{+1}_{-2} \times 10^{-3}$
$E(B − V)$ (mag)	1.97±0.10
R_V	3.26±0.10
M_V (mag) (adopted)	−6.8±0.5
d (kpc)	$5.6^{+1.5}_{-1.2}$

Note: [a] 2012 March 2; [b] 2013 April 27; [c] 2014 March 9.

rection (BC=−2.01 mag[7]) are nearly unchanged, so that we can assume no significant variations in the luminosity over time. The resulting SED well matches the photometry from optical to mid-infrared wavelengths, and no infrared excess is observed (see Fig. 6).

By converting the luminosity range into distances, we found that MN18 lies at a distance of $d\approx5.6^{+1.5}_{-1.2}$ kpc. The line of sight towards MN18 ($l\approx$321°) first crosses the Carina-Sagittarius Arm at $\approx$0.7–1.5 kpc and then the Crux-Scutum one at $\approx$3.6–4.4 kpc (Vallée 2014). Our distance estimate implies that MN18 is located either in the Crux-Scutum Arm or in the interarm region. In Section 6.4, we argue that the former possibility is more plausible. Note that the luminosity of MN18 and its R_* and $\dot{M}$ (given in Table 5) can be scaled to different distances as $\propto d^2$, $\propto d$ and $\propto d^{3/2}$, respectively (Schmutz, Hamann & Wessolowski 1989).

Using the FEROS spectra, we estimated the projected rotational velocity, $v\sin i$, of MN18. For this, we used the relations between the FWHMs of the He I $\lambda\lambda$4387, 4471 lines and $v\sin i$ given in Steele, Negueruela & Clark (1999). For FWHM(4388)=2.24±0.25 Å and FWHM(4471)=2.10±0.13 Å, we found $v\sin i\approx$94.1±10.5 km s^{-1} and 86.6±5.4 km s^{-1}, respectively, with a mean value of 90.4±5.9 km s^{-1}, which for i=60° (see Section 2) translates into the equatorial rotational velocity of v_{eq}=104±7 km s^{-1}. These estimates should be considered as an upper limit to the rotational velocity because the macroturbulence could contribute to the line broadening.

A summary of the stellar and extinction parameters is given in Table 5.

---

[5] This is an upper limit because the Hα line was in absorption in 2012.

[6] The filter functions were approximated for each filter system individually using Gaussian and boxcar functions with appropriate widths and wavelengths.

[7] Note that almost the same value of BC (−2.03 mag) follows from relation between BC and T_{eff} of B supergiants given in Crowther et al. (2006).
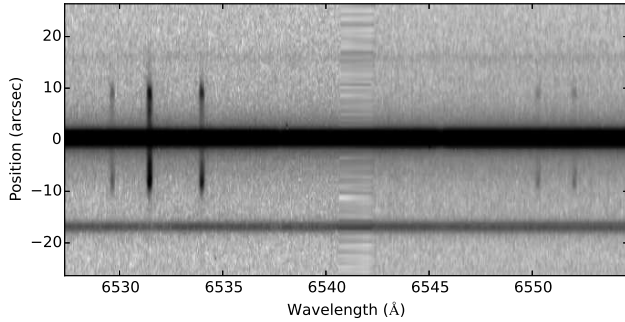
Figure 7. A part of the 2D high-resolution spectrum of the equatorial ring around MN18, showing nebular emission lines (from left to right) of [N II] $\lambda6548$, Hα, [N II] $\lambda6548$ and [S II] $\lambda\lambda6717$, 6731.

.

5 SPECTROSCOPY OF THE EQUATORIAL RING

5.1 Physical conditions and elemental abundances

As noted in Section 3.1, all SALT spectra were obtained with the slit oriented along the major axis of the equatorial nebula. In two-dimensional (2D) spectra the nebula appears as emission lines of Hβ, Hα, [N II] $\lambda\lambda6548$, 6584 and [S II] $\lambda\lambda6717$, 6731, visible on both sides of MN18. Note that in the region of the Hα line the nebula is more than 5 mag fainter than the star and therefore it does not affect the stellar photometry appreciably. A part of one of the two 2D high-resolution spectra is shown in Fig. 7. Besides the nebular spectrum and the spectrum of MN18, Fig. 7 also shows spectra of two other stars on the RSS slit, which are located at almost equal distances on both sides of MN18. In Section 6.4 we show that the brighter star is of late O-/early B-type.

The upper and bottom panels of Fig. 8 plot the nebular emission line intensities and their ratios along the slit. From the upper panel it follows that the nebula can be traced up to ±11 arcsec (at a ten per cent level of the Hα peak intensity) from MN18, which corresponds with the extent of the equatorial ring in the *Spitzer* and SHS images (see Fig. 2). This panel also shows that the line intensities peak at ≈8.5 arcsec from the star, which reflects the toroidal topology of the nebula.

The lower panel of Fig. 8 shows that the [N II] $\lambda6584$/Hα line ratio increases with distance from MN18 and peaks at the edge of the nebula. Using the prescription by Dopita (1973), one finds that [N II]/Hα is proportional to $n_{\mathrm{e}}^{-1}T_{\mathrm{e}}^{1/2}\exp(-21\,855/T_{\mathrm{e}})$, where n_{e} and T_{e} are the electron number density and temperature, respectively. Thus, the behaviour of [N II] $\lambda6584$/Hα could be explained (at least in part) by the temperature increase of the photoionized gas towards the outer edge of the nebula (caused by the hardening of the ionizing radiation field), provided that the density is constant throughout the nebula.

One-dimensional spectra (1D) of the nebula were extracted by summing up, without any weighting, all rows from the area of an annulus with an outer radius of 10 arcsec centred on MN18 and the central ±3 arcsec excluded. Both low- and high-resolution 1D spectra of the nebula are

Table 6. Line intensities of the MN 18 nebula.

λ_0(Å) Ion	F(λ)/F(Hβ)	I(λ)/I(Hβ)
4861 Hβ	1.000±0.236	1.000±0.249
6548 [N II]	7.083±1.183	0.578±0.111
6563 Hα	36.750±6.136	2.947±0.564
6584 [N II]	21.792±3.647	1.705±0.327
6717 [S II]	3.708±0.631	0.248±0.049
6731 [S II]	3.750±0.637	0.247±0.049
C(Hβ)	3.30±0.22	
$E(B-V)$	2.24±0.15 mag	
n_{e}([S II])	560^{+450}_{-270} cm^{-3}	

presented in Fig. 9. The emission lines detected in the spectra were measured using the programs described in Kniazev et al. (2004). Table 6 lists the observed intensities of these lines normalized to Hβ, F(λ)/F(Hβ), the reddening-corrected line intensity ratios, I(λ)/I(Hβ), and the logarithmic extinction coefficient, C(Hβ), which corresponds to $E(B-V)$=2.24±0.15 mag. In Table 6 we also give the electron number density derived from the intensity ratio of the [S II] $\lambda\lambda6716$, 6731 lines, n_{e}([S II]). The obtained value is comparable to densities derived for equatorial rings of other bipolar nebulae around blue supergiants and cLBVs (see Section 6.2). Both C(Hβ) and n_{e}([S II]) were calculated under the assumption that $T_{\mathrm{e}} = 10^4$ K. For lower temperatures their values do not change much, e.g. C(Hβ)=3.27 and $n_{\mathrm{e}} = 510$ cm^{-3} if T_{e}=7000 K.

The electron number density could also be derived from the surface brightness of the equatorial ring in the Hα line, $S_{\mathrm{H}\alpha}$, measured on the SHS image (cf. equation (4) in Frew et al. 2014):

$$n_{\mathrm{e}} \approx 5\,\mathrm{cm}^{-3}\left(\frac{l}{1\,\mathrm{pc}}\right)^{-0.5}\left(\frac{S_{\mathrm{H}\alpha}}{1\,\mathrm{R}}\right)^{0.5}e^{E(B-V)}, \qquad (1)$$

where l is the line of sight thickness of the ring and $1\,\mathrm{R}{\equiv}1\,\mathrm{Rayleigh}{=}5.66{\times}10^{-18}$ erg cm^{-2} s^{-1} arcsec^{-2} at Hα (here we assume that n_{e} is constant within the ring and $T_{\mathrm{e}} = 10^4$ K).

Using equations (1) and (2) in Frew et al. (2014) and the flux calibration factor of 7.2 counts pixel^{-1} R^{-1} from their table 1, and adopting the observed [N II] to Hα line intensity ratio of 0.79 from Table 6 (here [N II] corresponds to the sum of the $\lambda6548$ and $\lambda6584$ lines), we obtained the peak surface brightness of the northeastern (brightest) half of the ring (corrected for the contribution from the contaminant [N II] lines) of $S_{\mathrm{H}\alpha}{\approx}120$ R. Using equation (1) with $E(B-V)$=1.97 mag and $l{\approx}0.47$ pc (the line of sight thickness of the torus), one finds $n_{\mathrm{e}}{\approx}570$ cm^{-3}, which agrees well with n_{e}([S II]) given in Table 6.

To obtain an order of magnitude estimate of the mass of the equatorial ring, M_{ring}, we assume that the ring has a toroidal geometry with the major and minor radii of R=6.5 arcsec (≈0.17 pc) and r=4.5 arcsec (≈0.12 pc), respectively, and that its material is fully ionized and homogeneous. In doing so, one finds $M_{\mathrm{ring}}{\approx}1$ M$_\odot$. The actual value of M_{ring} could be higher if the ionized gas encloses neutral and, correspondingly, more dense material.
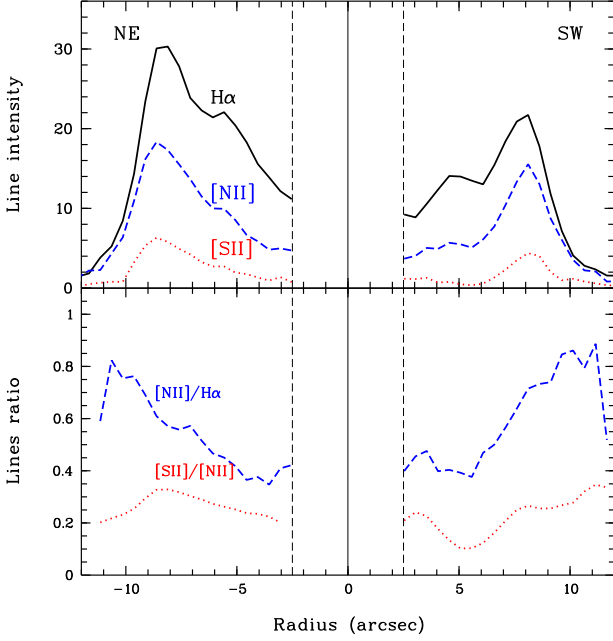
The [N II] and [S II] line intensities can be used to

Figure 8. Variation of emission line relative fluxes and their ratios along the slit. The solid vertical line corresponds to the position of MN18, while vertical dashed lines at $\pm 2.5''$ from the solid line mark the area where no nebular emission was detected. NE−SW direction of the slit is shown. *Upper panel:* The relative fluxes of the Hα, [N II] $\lambda 6584$ and [S II] $\lambda 6717+\lambda 6731$ lines after continuum subtraction. *Bottom panel:* [N II] $\lambda 6584$/Hα and [S II] $\lambda 6717+\lambda 6731$/[N II] $\lambda 6584$ line ratios.
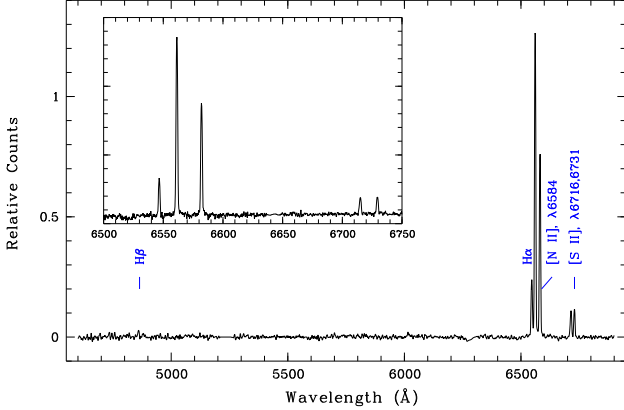

Figure 9. 1D low-resolution spectrum of the equatorial nebula around MN18. The insert shows a part of the high-resolution spectrum of the nebula taken on 2013 April 27.

estimate the nitrogen to sulphur abundance ratio, which is almost independent of n_e and T_e, provided that $n_e \leqslant 1000\,\mathrm{cm}^{-3}$ and $T_e \leqslant 10^4$ K. In this case, the abundance ratio is given by (see Benvenuti, D'Odorico & Peimbert 1973 and references therein):

$$\frac{N(\mathrm{N}^+)}{N(\mathrm{S}^+)} = 3.61 \frac{I(6584)}{I(6716+6731)} . \qquad (2)$$

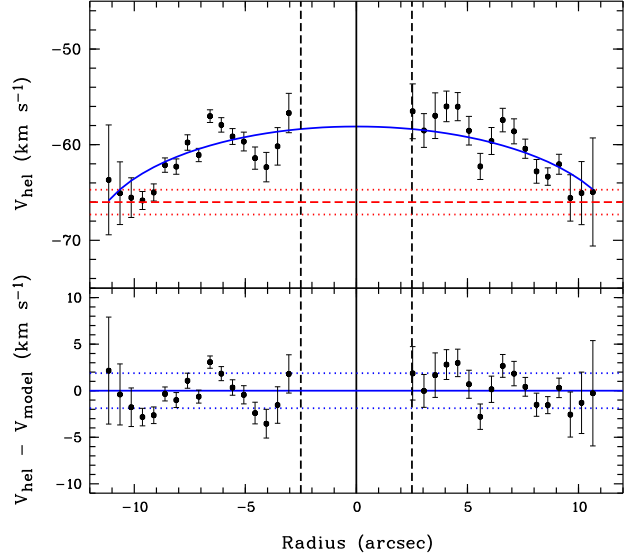Using   equation (2)   and   Table 4,   one   finds

Figure 10. *Upper panel:* Hα heliocentric radial velocity distribution along the slit. The solid vertical line corresponds to the position of MN18, while the vertical dashed lines at $\pm 2.5''$ from the solid line mark the area where no nebular emission was detected. The model fit is shown as a (blue) solid line. The (red) dashed and dotted horizontal lines show, respectively, the systemic velocity of the equatorial ring and its error margins. *Bottom panel:* The difference between the observed and model radial velocity distributions. The mean residual velocity and its errors are shown with the (blue) solid and dotted lines, respectively.

$N(\mathrm{N}^+)/N(\mathrm{S}^+) \approx 12.43^{+6.05}_{-4.04}$, which is $\approx 2.4^{+1.2}_{-0.8}$ times larger than the solar value of 5.12 (Asplund et al. 2009). Since the sulfur abundance is not expected to change during stellar evolution, one can argue that the high N to S ratio exists because of an elevated nitrogen abundance in the line-emitting material. Thus, using the solar N and S abundances from Asplund et al. (2009), one finds a N abundance of the ring of $\log(\mathrm{N/H})+12 = 8.21$.

5.2 The position–velocity diagram and kinematics of the equatorial ring

Fig. 10 plots the distribution of the heliocentric radial velocity of the Hα line, v_{hel}, along the slit, calculated using the method and programs described in Zasov et al. (2000). The systematic shifts originating from the RSS flexure were excluded by taking into account the closest bright night sky line. Finally, only those velocity measurements were used which satisfy the criteria $\mathrm{S/N} > 3$ and $\sigma_v < 6\,\mathrm{km\,s}^{-1}$.

To estimate the systemic velocity of the equatorial ring, v_{sys}, and its expansion velocity, v_{exp}, we fit the observed distribution of v_{hel} with the model:

$$v_{\mathrm{hel}} = v_{\mathrm{exp}} \cos \alpha + v_{\mathrm{sys}} , \qquad (3)$$

where v_{exp} and v_{sys} are free parameters, and α is the angle between the line of sight and v_{exp} at each point of the ring. The result of the fit is shown as a (blue) solid line in the upper panel of Fig. 10. The (red) dashed and dotted horizontal lines show, respectively, the derived v_{sys} of $-66.0\,\mathrm{km\,s}^{-1}$ and its error margins ($\pm 1.3\,\mathrm{km\,s}^{-1}$). We also

found $v_{exp} = 7.9 \pm 1.2$ km s^{-1}. The difference between the observed and model velocity distributions (the residual velocity hereafter) is shown in the bottom panel of Fig. 10, where the (blue) solid and dotted lines indicate, respectively, the mean residual velocity of -0.05 km s^{-1} and $\pm 1\sigma$ of the mean (± 1.8 km s^{-1}). The residual velocity distribution does not show any systematics, which allows us to set an upper limit of 1.8 km s^{-1} on the rotational velocity of the ring.

The radius of the ring of $r=0.29$ pc together with v_{exp} yield the kinematic age of the ring of $t_{kin}=r/v_{exp}\approx 3.7 \times 10^4$ yr. Assuming that the equatorial ring and bipolar lobes are the result of the same episode of enhanced mass loss from MN18 (i.e. their t_{kin} are the same; cf. Brandner et al. 1996b), one finds that the lobes should expand at ≈ 60 km s^{-1}. Using M_{ring} from Section 5.1 and t_{kin}, one can also find an order of magnitude "kinematic" estimate of $\dot{M}$ during this episode, i.e. $\dot{M}_{kin} \sim M_{ring}/t_{kin} \approx 2.7 \times 10^{-5}$ M$_\odot$ yr^{-1}, which is about two orders of magnitude higher than the present-day values (see Table 5). The discrepancy between the mass-loss rates would be somewhat smaller if the expansion of the equatorial ring was faster initially. (Correspondingly, the expansion velocity of the lobes would be smaller as well.) On the other hand, the duration of the high mass loss episode could be shorter than t_{kin}, which would result in an even higher $\dot{M}_{kin}$.

6 DISCUSSION

In Section 1, we noted the existence of a class of Galactic and extragalactic hourglass-like nebulae associated with blue supergiants and mentioned seven known members of this class. One of them – the three-ring nebula associated with the blue supergiant Sk$-69°202$ (the progenitor star of the SN 1987A) – was formed shortly ($\sim 10^4$ yr) before the star exploded as a supernova. Currently, one can observe how the supernova blast wave interacts with the equatorial ring of the nebula (Sonneborn et al. 1998; Sugerman et al 2002; Gröningsson et al. 2008; Fransson et al. 2015). It is also believed that LBVs could be immediate precursors of supernova explosions (e.g. Kotak & Vink 2006; Groh et al. 2013; Justham et al. 2014). Thus, one can expect that some other massive stars with bipolar nebulae will soon explode as supernovae and that the appearance of their young (meaning from decades to centuries old) diffuse supernova remnants would be affected by the dense material of the nebulae. It is therefore worth to compare the derived parameters of MN18 with those predicted by stellar evolutionary models (e.g., Brott et al. 2011; Ekström et al. 2012) to determine the evolutionary status of this star and thereby to understand whether or not it is close to explode as well. Knowing the evolutionary status of MN18 would also allow us to constrain the mechanism for the origin of the bipolar nebula around this star, which in turn would help to better understand the origin of bipolar nebulae around other massive stars.

6.1 Evolutionary status of MN18

The range of luminosities derived for MN18 in Section 4.2 corresponds to the initial mass, M_{init}, of this star of $\approx 30 \pm 10$ M$_\odot$. Using the grid of rotating main sequence stars by Brott et al. (2011), we found that the main parameters

of MN18 (temperature, luminosity, gravity and CNO abundances) can be matched very well with models with M_{init} in the above range, provided that the initial rotational velocity of the star, v_{init}, was of ~ 200–400 km s^{-1}. For example, the model of a 30 M$_\odot$ star with $v_{init} = 321$ km s^{-1} predicts that after ≈ 5.5 Myr the star would have the following parameters: $T_{eff} \approx 21.0 \pm 0.5$ kK, $\log(L/L_\odot) \approx 5.41$, $R_* \approx 38 \pm 2$ R$_\odot$, $\log g \approx 2.70 \pm 0.05$ and a current rotational velocity of $\approx 110 \pm 10$ km s^{-1}. The CNO abundances of this star would be $\approx 6.3 \times 10^{-4}$, 1.6×10^{-3} and 3.4×10^{-3}, respectively. All these parameters are in good agreement with those derived for MN18 (see Table 5). The models with low v_{init} also match very well the T_{eff}, $\log(L/L_\odot)$ and $\log g$ values of MN18, but their CNO abundances differ significantly. Specifically, the nitrogen abundances predicted by these models are much lower than what follows from our spectral modelling.

Similarly, we found that the rotating models by Ekström et al. (2012) also fit well the parameters of MN18 provided that this star just left the main sequence, while in the case of a star undergoing a blue loop evolution the CNO abundances predicted by the models differ significantly from those of MN18. The non-rotating models by Ekström et al. (2012) do not fit the CNO abundances of MN18 as well. Proceeding from this, one might conclude that MN18 is a redward evolving star, which has only recently become a blue supergiant (cf. Gvaramadze et al. 2014a). This conclusion agrees with the suggestion by Lamers et al. (2001) that LBV nebulae could be formed already at the end of the main sequence phase and that their enhanced nitrogen abundances are due to rotationally induced mixing in their underlying stars. Similar suggestions were put forward by Smartt et al. (2002) and Hendry et al. (2008) to explain the CNO abundances of the bipolar nebula around Sher 25.

The duplicity of massive stars provides another clue for understanding the origin of enhanced N abundance in main sequence stars because accretion of CNO-processed material from the mass donor star or merger of the binary components can enhance the surface N abundance of the mass gainer star or the merger product, respectively, by a factor of several even in the absence of rotational mixing[8] (Langer 2012; Glebbeek et al., 2013). As follows from the studies by Mason et al. (2009), Sana & Evans (2011) and Chini et al. (2012), the majority of massive stars are members of close binary systems. Furthermore, according to Sana et al. (2012), about 70 per cent of all massive stars are strongly affected by binary interaction during their lifetimes through the mass transfer, common envelope evolution or merger, and for more than half of them the interaction takes place already during the main sequence phase (see also de Mink et al. 2014). All of these types of binary interaction can enhance the surface N abundance already during the main sequence phase, and are also the likely culprits of the production of substantial mass loss in the equatorial plane.

Thus, MN18 could be a mass gainer from a Case A or Case B system, and as such it could either be rejuvenated or not. In the first case there would be little difference to

---

[8] Models taking into account rotational mixing in the mass gainers show that the N abundance can additionally be enhanced by a factor of 3 (Langer et al. 2008).

single star evolution, while in the second one the star at its position in the Hertzsprung-Russell diagram could either be core hydrogen or core helium burning (Braun & Langer 1995; Justham et al. 2014). The latter possibility, however, is less likely because the N abundance of the star would be much higher than what we found for MN18.

To summarize, the above considerations suggest that MN18 is near the end of the main sequence phase, which makes it unlikely that this star will soon explode as a supernova.

6.2 Origin of the bipolar nebulae

Now we discuss the origin of bipolar nebulae around MN18 and other massive stars. The rotational symmetry of these nebulae implies that the stellar rotation plays a significant, if not a decisive, role in their origin.

6.2.1 Single star scenarios

Lamers et al. (2001) proposed that at the end of the main sequence the initially rapidly rotating stars may reach the limit of hydrostatic stability (Ω-limit; Langer 1997, 1998) in their outer equatorial layers, where the joint action of the centrifugal force and the radiation pressure balances the gravity (cf. Langer, Garía-Segura & Mac Low 1999). This may result in ejection of a large amount of mass (up to several $M_\odot$) mainly in the equatorial plane. The ejection process could be recurrent with time intervals of $\sim 10^3 - 10^4$ yr, which are related to the thermal time-scale of the stars. Correspondingly, the stellar wind in between the ejections could be collimated in the polar direction by the presence of the dense equatorial material.

To reach the Ω-limit the star should be luminous enough to arrive at or exceed its Eddington limit in the course of its lifetime and/or be a rapid rotator. For single stars the first condition could be satisfied during the advanced evolutionary phases of very massive ($\gtrsim 50$ $M_\odot$) stars when their masses are considerably reduced due to the extensive stellar wind. Such stars can achieve the Ω-limit even if they are slow rotators (e.g. Langer & Heger 1998). The resulting enhanced mass loss of these stars is almost spherically symmetric and, correspondingly, the circumstellar nebulae around them should be almost spherical as well. In the case of very rapid rotators, the Ω-limit could be reached already during the main sequence. This is conceivable even for those stars which never approach the Eddington limit during their lifetime. Correspondingly, the mass loss from these stars would be highly aspherical, with a slow and dense wind at latitudes close to the equator and a fast and more tenuous one in the polar direction. These stars would produce elongated or bipolar nebulae.

Interestingly, the Brott et al.'s models predict that a $20-30$ $M_\odot$ star with $v_{\rm init} \approx 500-600$ km s^{-1} can achieve the Ω-limit by the end of the main sequence, which results in a strong mass loss with $\dot{M}$ of $\gtrsim 10^{-4}$ $M_\odot$ yr^{-1}. But the higher $v_{\rm init}$, the stronger the mixing, the longer the duration of the main sequence phase and the bluer the star. Correspondingly, it takes longer for the star's $T_{\rm eff}$ to decrease to 21 kK. The prolonged rotational mixing in turn results in CNO abundances much different from those derived from our spectral analysis.

The question on whether the surface velocity of single stars may hit critical rotation during the main sequence evolution was studied in detail by Ekström et al. (2008). They computed stellar models of various $M_{\rm init}$, $v_{\rm init}$ and metallicities, and found that the Ω-limit could be reached by B stars with $v_{\rm init}$ in the upper tail of the initial rotational velocity distribution. This could be responsible for the origin of the Be phenomenon. Ekström et al. (2008) also found that much greater mass loss from more massive stars at high (e.g. solar) metallicities prevents these stars from reaching the critical rotation.

Heger & Langer (1998) proposed a mechanism which may spin-up the surface layers of rotating single stars to critical rotation after they leave the red supergiant branch. It was suggested that this mechanism may result in significant rotation of the progenitor star of the SN1987A (which performed a blue loop just before the supernova explosion) and thereby in the origin of the equatorial ring around it. The CNO abundances of the material ejected by a post-red supergiant star, however, would significantly differ from those of MN18 (see Section 6.1).

Another possibility to increase mass loss rates of single stars is based on the bi-stability in the radiation driven winds of supergiants near the spectral type B1 (Pauldrach & Puls 1990; Lamers & Pauldrach 1991), which is manifested in a drastic change in the ionization states of Fe when $T_{\rm eff}$ drops a little below some critical value (≈ 21–25 kK; Vink, de Koter & Lamers 1999). This change leads to a factor of 2 decrease in v_∞, from $v_\infty/v_{\rm esc} \approx 2.6$ for supergiants of types earlier than B1 to $v_\infty/v_{\rm esc} \approx 1.3$ for B supergiants of later types (Lamers et al. 1995), and in a factor of several increase in $\dot{M}$ (Lamers et al. 1995; Vink et al. 1999). The increase of $\dot{M}$ caused by the bi-stability jump could be responsible for the ejection of shells by the prototype LBV P Cygni (Pauldrach & Puls 1990) and the observed steep drop in the rotational velocities of massive stars at $T_{\rm eff}$ of 22 kK (Vink et al. 2010).

More importantly, the enhanced mass loss caused by the bi-stability mechanism could be asymmetric if the star is a rapid rotator. In this case, the gravity darkening (the von Zeipel effect) leads to a lower $T_{\rm eff}$ at the equator (e.g. Maeder 1999) and the bi-stability jump first occurs near the equator as well. This in turn results in enhanced mass loss at low stellar latitudes. Lamers & Pauldrach (1991) and Lamers et al. (1995) suggested that the bi-stability jump in the winds of rapidly rotating early B-type supergiants could be responsible for the origin of dense equatorial outflows (excretion disks) around B[e] stars. The detailed study of this possibility by Pelupessy, Lamers & Vink (2000), however, showed that the bi-stability mechanism can produce only about a four-fold increase in $\dot{M}$, which is not enough to explain the equator to pole density contrast of a factor of ≈ 100 observed for the winds of B[e] stars. It is therefore doubtful that the bi-stability jump alone could explain the about two order of magnitude difference between $\dot{M}$ derived from our spectral modelling of MN18 (see Table 5) and $\dot{M}$ required to produce the equatorial ring around this star (see Section 5.2).

To conclude, although we cannot exclude the possibility that some single massive stars can hit critical rotation in the course of their evolution (resulting in massive equatorial outflows), we believe that the origin of the equatorial ring

around MN18 is more likely because this star is or was a member of a close binary system.

6.2.2 Binary star scenarios

The binary population synthesis modelling by de Mink et al. (2013) suggests that about 20 per cent of massive main sequence stars should be rapid ($> 200 \mathrm{~km \, s^{-1}}$) rotators because of mass transfer and mergers in close binary systems. About 2 per cent of these stars are expected to have very high ($> 400 \mathrm{~km \, s^{-1}}$) rotational velocities (with the most extreme cases reaching $\approx 600 \mathrm{~km \, s^{-1}}$) of which a quarter are the merger remnants. de Mink et al. (2013) noted that their predicted distribution of rotational velocities of main sequence stars agrees well with the observed one, which points to the possibility that mass transfer and mergers are the main causes for the rapid rotation of massive stars (cf. Packet 1981; Langer et al. 2003; Dufton et al. 2011). It is tempting therefore to speculate that these two binary interaction processes are the main causes for the origin of nearly critically rotating stars and equatorial outflows from them.

The mass transfer in binary systems may not only spin-up the mass gainers, but under proper conditions it could also result in the origin of circumbinary disk-like structures by means of the common envelope ejection (e.g. Morris 1981), mass loss through the second Lagrange point (e.g. Livio, Salzman & Shaviv 1979; Petrovic, Langer & van der Hucht 2005; Smith et al. 2011), and focusing of the primary's wind towards the orbital plane by the gravitational field of the companion star (e.g. Fabian & Hansen 1979; Mastrodemos & Morris 1999). Similarly, the binary mergers can not only produce the rapidly rotating stars, but also result in mass ejection ($\sim$10 per cent of the binary mass; Suzuki et al. 2007), which is mainly concentrated in the binary's equatorial plane. Moreover, the instant mass loss during the merger event may bring the merger product to the Eddington limit, which in turn would result in a copious mass loss by stellar wind.

If the origin of the equatorial ring around MN18 is indeed caused by the equatorial mass loss from either a nearly critically rotating mass gainer or a merger remnant, then the present moderate rotational velocity of this star would imply that the star has suffered significant angular momentum loss on a time-scale of $\leqslant t_{\mathrm{kin}}$. The most efficient mechanisms for the spin down of (single) massive stars is the magnetic braking via a magnetized wind (Poe, Friend & Cassinelli 1989; ud-Doula, Owocki & Townsend 2009), which for stellar magnetic fields of $\sim 10^3 - 10^4$ G and sufficiently high $\dot{M}$ can result in spin-down time-scales as short as $\sim 10^4$ yr. It is not clear whether initially single stars can simultaneously possess such high magnetic fields and be rapid rotators, but it is believed that very strong large-scale magnetic fields can intermittently be created because of the strong shear in merging binary systems (Langer 2012; Wickramasinghe, Tout & Ferrario 2014). Such magnetic fields can brake the rapid rotation of the merger remnants through dynamical mass loss. Polarimetric observations of MN18 and other stars with bipolar nebulae would be of great importance to check whether they possess large-scale magnetic fields of strength of $\sim$100–1000 G, which are not typical of the majority of massive main sequence stars (e.g. Wade et al. 2014; Morel

et al. 2015) and whose origin can be the consequence of binary merger.

In Section 5.2, we assumed that the kinematic ages of the equatorial ring and bipolar lobes of the nebula around MN18 are the same (i.e. both components of the nebula were formed simultaneously). But it is quite possible that the ring was formed in the first instance (e.g. because of a dynamical mass ejection caused by the binary merger) and that later on its dense material collimated the stellar wind into bipolar lobes. If so, then pure ring-like nebulae should exist whose central stars still have had no time to blow-up pronounced bipolar lobes and which still might be fast rotators. Indeed, several examples of such rings exist. One of them, named [GKF2010] MN109 in the SIMBAD data base, encircles the candidate blue supergiant 2MASS J19281457+1716230 (Phillips & Ramos-Larios 2008). This ring is best visible at $8 \, \mu$m (see the right-hand panel of Fig. 11), while at $24 \, \mu$m there are no signatures of an extended bipolar outflow. Another example, known as [GKF2010] MN56, is associated with the cLBV MN56. In Fig. 12, we present for the first time the K-band spectrum of this star obtained with the ISAAC spectrograph on the Very Large Telescope (VLT) during our observing run in 2010[9]. The spectrum shows strong emission lines of H, He I, Fe II and Mg II and is almost identical to that of the cLBV HD 316285 (see fig. 2 in Hillier et al. 1998). [GKF2010] MN56 also has a clear-cut ring-like morphology with a "horn" attached to the south-east edge of the ring (see the right-hand panel of fig. 4 in Paper I for the IRAC $5.8 \, \mu$m image of this structure). The presence of the horn suggests that the stellar wind already starts to be collimated into bipolar lobes. The saturated $24 \, \mu$m image of [GKF2010] MN56 (see the left-hand panel of fig. 4 in Paper I) did not allow us to discern the horn, but it also did not show signatures of a more extended bipolar outflow. High-resolution spectroscopy of 2MASS J19281457+1716230 and MN56 would be desirable to determine the rotational velocities of these two stars, as well as the evolutionary status of the former one.

Binary population studies suggest that the rate of massive binary mergers in the Galaxy is $\sim$10–20 per cent of the Galactic supernova rate, which corresponds to one per 200 yr (Langer 2012). Assuming that all mergers result in the formation of ring-like or bipolar nebulae and that the dispersion time-scale of these nebulae is $\sim 10^4$ yr, one finds that our Galaxy should contain about 100 such nebulae. The actual number of these nebulae however should be much smaller because the majority ($\approx$80 per cent; Gies 1987) of massive stars reside in their parent star clusters where the stellar winds and ionizing emission of neighbouring hot massive stars could prevent the formation of discernible circumstellar nebulae. This inference could be supported by the fact that all massive stars with known well-shaped (bipolar or ring-like) nebulae are located either at the periphery of their parent star clusters or in the field, and therefore are likely runaway stars (Gvaramadze et al. 2012a,b; 2014b).

---

[9] Full details of these observations will be presented elsewhere, while some preliminary results could be found in Stringfellow et al. (2012a,b).
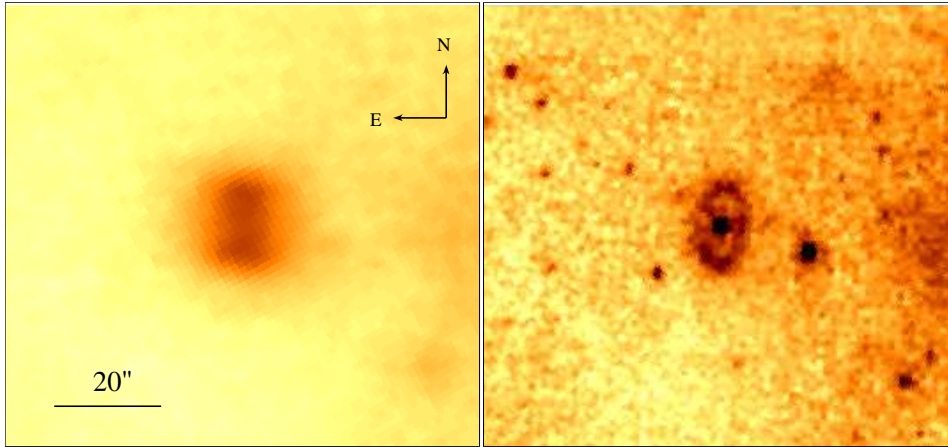
Figure 11. *Spitzer* MIPS 24 μm (left) and IRAC 8 μm images of a ring-like nebula around the possible blue supergiant 2MASS J19281457+1716230.
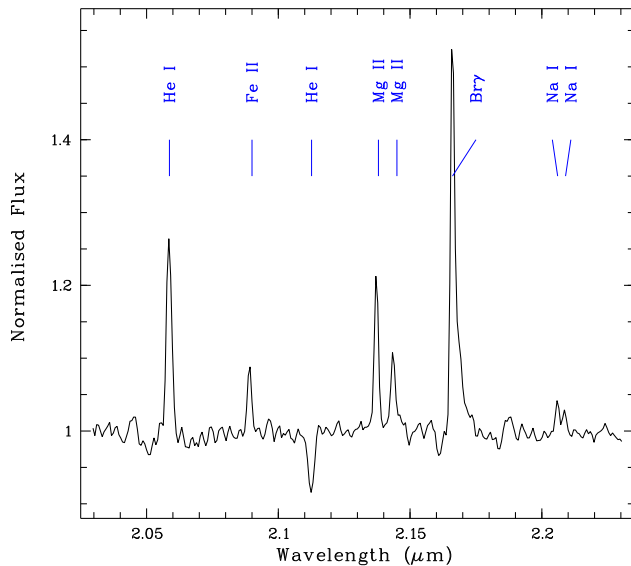

Figure 12. Normalized VLT/ISAAC K-band spectrum of the cLBV MN56 with principal lines indicated.

6.3 MN18 and other B supergiants with bipolar nebulae

All but one (MN13) of seven hourglass-like nebulae around B supergiants mentioned in Section 1 are visible (at least partially) at optical wavelengths, and five of them were studied by means of optical spectroscopy[10]. In Table 7, we compare the main parameters of the central stars and equatorial rings of these five nebulae.

Table 7 shows that the luminosities of the stars associated with bipolar nebulae span a large range, from $\log(L/L_\odot)$= 4.7 to 5.8 (with the luminosity of MN18 being close to the median value of ≈5.3). From this one can conclude that the stellar luminosity (or M_{init}) is not a decisive factor in formation of bipolar nebulae, which is expected if the nearly critical rotation is the main reason for the origin of these nebulae. In this regard, it is worthy to note that some PNe also possess the hourglass-like morphology, whose origin is most likely due to binary interactions (e.g. Corradi & Schwarz 1993; Sahai et al. 1999; De Marco 2009).

One can also see that T_{eff} values span quite a large range as well, from 13 to 22 kK, which might be considered as an indication that the bi-stability mechanism may not contribute to the origin of at least some of the bipolar nebulae. This inference, however, could be inconclusive because T_{eff} of bona fide LBVs can vary in the same range on time scales as short as several years (e.g. Stahl et al. 2001; Groh et al. 2009). One cannot therefore exclude the possibility that T_{eff} of Sk−69°202 and HD 168625 were close to the bi-stability limit during the formation of nebulae around these stars.

The axial symmetry of the bipolar nebulae suggests that the tilt angles of their equatorial rings are equal to those of the rotational axes of the central stars. This allows one to estimate the rotational velocities for those stars whose projected rotational velocities are known. Table 7 shows that none of these four stars are rapid rotators[11]. Thus, if the origin of the equatorial rings is due to the nearly critical rotation of their underlying stars, then the spin-down time-scales of these stars should be shorter than t_{kin} of the equatorial rings, all of which are $\sim 10^4$ yr. It is reasonable to associate this drastic spin down with a brief episode of very high $\dot{M}$ (e.g. Heger & Langer 1998), which is much higher than the current values of $\dot{M}$ and perhaps even higher than the "kinematic" ones, $\dot{M}_{kin} \sim M_{ring}/t_{kin}$.

Table 7 also shows that the linear sizes of all equatorial rings are almost the same: 0.2−0.3 pc. The largest value of 0.3 pc was obtained for the equatorial ring around MN18 under the assumption that the distance to this object is 5.6 kpc. At a shorter distance of ≈4.4 kpc (allowed by the error margins of d; see also Section 6.4) the radius of the

---

[10] There are no reported spectroscopic observations of the equatorial belt (visible in optical light; Marston & McCollum 2008) of the bipolar nebula around the cLBV MWC 349A.

[11] There is no information on the projected rotational velocity of the progenitor star of the SN1987A.

ring would be similar to those of other equatorial rings. The similarity in size of the rings produced by stars of different M_{init} and evolutionary status, however, is most probably a coincidence, because it is difficult to imagine any viable mechanism for constraining it.

The number densities of all equatorial rings are also about the same ($\sim 1000\,\mathrm{cm}^{-3}$) except of the ring around Sk$-69°202$, for which an order of magnitude higher value was derived from the fading of the [O III] $\lambda5007$ emission line (Plait et al. 1995). The masses of the equatorial rings range from ≈0.1 to $1\,M_\odot$ with the lowest mass belonging to the ring around Sk$-69°202$. This ring, however, might be more massive if we see only its inner-faced ionized part (e.g. Plait et al. 1995; cf. Fransson et al. 2015).

Finally, Table 7 gives also the nitrogen abundances (by number) of the equatorial rings. In the Sk$-69°202$ ring the N abundance is a factor of 20 greater than the LMC in general (7.14 dex; Russell & Dopita 1992), which is consistent with the fact that the material of this ring was ejected during the final stage of the evolution of Sk$-69°202$. The Sher 25 ring is also greatly enriched with nitrogen as compared to the background H II region NGC 3603 and the Sun, respectively, by factors of ≈30 and 12 (Hendry et al. 2008). Although this overabundance could be interpreted as an indication that Sher 25 have evolved through the red supergiant stage (Brandner et al. 1997a,b), Hendry et al. (2008) argued that M_{init} of Sher 25 of $\sim50\,M_\odot$ rather implies that this star did not experience this stage at all. Instead, Hendry et al. (2008) suggested that the enhanced N abundance is because of rotationally induced mixing while the star was on the main sequence. Mass accretion or a merger in a binary system might be responsible for this enhancement as well (cf. Section 6.1). The abundances of the rings produced by HD 168625 and MN18 exceed the solar abundance by a factor of few, while that of the [SBW2007] 1 ring is subsolar. It is therefore likely that the underlying stars of these three rings have not yet passed through the red supergiant stage and that all these rings were formed at the end of the main sequence stage or soon after it (cf. Lamers et al. 2001; Smith 2007; Smith et al. 2007; Gvaramadze et al. 2014a). The largely different N abundances of the equatorial rings imply that blue supergiants are capable to produce them in very different evolutionary stages, from the main sequence stage up to the pre-supernova stage. MN18 adds to the evidence that multiple ring nebulae could be formed rather early during the stellar evolution.

6.4 MN18 and Lynga 3

Is Section 2, we mentioned that Lynga (1964a) listed MN18 among the members of the newly identified open star cluster Lynga 3. Lynga (1964b) noted that the cluster is strongly reddened, which did not allow him to estimate the interstellar extinction and the distance to the cluster.

A literature search revealed three subsequent studies of Lynga 3, based either on infrared or optical photometry. Carraro et al. (2006) constructed a colour-magnitude diagram of what they assumed to be a cluster using their own CCD BVI photometry and did not find any significant difference with respect to a comparison field. This led them to conclude that "Lynga 3 is not a cluster, but an overdensity of a few bright stars probably located inside the Carina arm". It

turns out, however, that they confused the 1950 epoch coordinates with the 2000 epoch ones, which resulted in more than $0°\!.5$ offset between the group of stars they analyzed and the centre of the cluster given in Lynga (1964a,b). Moreover, the inspection of the finding chart of Lynga 3 given in fig. 13 of Lynga (1964a) revealed that the geometric centre of the putative cluster is offset by about $5'\!.5$ from the cluster's position listed in Lynga (1964a,b; see tables V in these papers). This explains why Carraro et al. (2006) came to the conclusion that Lynga 3 is not a true cluster.

More recently, Lynga 3 was studied by Kharchenko et al. (2013) and Dias et al. (2014), who used photometric and proper motion measurements from different catalogues to evaluate the membership probabilities for individual stars in the cluster region and to derive the distance to and age of the cluster. Although the coordinates of the cluster given in these two references are in a quite good agreement with each other (as well as with the position of the cluster's geometric centre implied by the finding chart in Lynga 1964a), the obtained distance estimates, 4.2 kpc (Kharchenko et al. 2013) and 1.4 kpc (Dias et al. 2014), differ from each other drastically. Moreover, the age estimates of $\log t = 8.92$ (Kharchenko et al. 2013) and 8.55 (Dias et al. 2014) are much older than the age of MN18 of $\log t \approx 7$ (see Section 6.1). Since this huge age difference cannot be explained by rejuvenation of MN18 because of mass transfer or merger in a binary system, it is reasonable to assume that MN18 and the putative star cluster are projected by chance along the same line-of-sight. This raises the question where the parent cluster of MN18 is?

A possible answer to this question is that MN18 is a runaway star, which was ejected and arrived at its current position from a nearby massive star cluster (cf. Gvaramadze, Pflamm-Altenburg & Kroupa 2011; Gvaramadze et al. 2012a). The runaway status of this star is suggested by proper motion measurements given in the SPM 4.0 (Girard et al. 2011) and UCAC4 (Zacharias et al. 2013) catalogues (see Table 8). Using these measurements, v_{sys} derived in Section 5.2, the Solar galactocentric distance $R_0 = 8.0$ kpc and the circular Galactic rotation velocity $\Theta_0 = 240$ km s^{-1} (Reid et al. 2009), and the solar peculiar motion $(U_\odot, V_\odot, W_\odot) = (11.1, 12.2, 7.3)$ km s^{-1} (Schönrich, Binney & Dehnen 2010), we calculated the peculiar transverse (in Galactic coordinates) velocity, v_l and v_b, the peculiar radial velocity, v_r, and the total space velocity, v_*, of MN18 (see Table 8). To take into account uncertainties in the distance estimate, we adopted three values of the distance: $d = 4.4, 5.6$ and 7.1 kpc (see Section 4.2). For the error calculation, only the errors of the proper motion and the systemic velocity measurements were considered.

From Table 8 it follows that if the SPM 4.0 and UCAC4 proper motion measurements are correct then MN18 is a high-velocity runaway star, moving almost along the Galactic plane and the plane of sky. In this case, the parent cluster of MN18 would be at $\sim15°$–$25°$ from the current position of the star (i.e. at $l \approx 336°$–$346°$), provided that it was ejected at the very beginning of the cluster's dynamical evolution (i.e. ~5–10 Myr ago). It should be noted, however, that although the high space velocity derived for MN18 is not unusual for single runaway OB stars, it would be unrealistically high if this star have been ejected as a binary (cf. Section 6.2). Moreover, the ram pressure of the interstellar medium due

Table 7. Blue supergiants and cLBVs with hourglass-like circumstellar nebulae.

	Sk−69°202	Sher 25	HD 168625	[SBW2007] 1	MN18
Spectral type	B3 I[1]	B1.5 Iab[2]	B6 Iap[3]	B1 Iab[4]	B1 Ia
$\log(L/\,\mathrm{L}_\odot)$	≈5[5]	5.8[6]	5.0−5.4[7]	4.7[8]	5.4
T_{eff} (kK)	16[5]	22[6]	12−15[7]	21[8]	21
$\dot M (10^{-7}\,\mathrm{M}_\odot\,\mathrm{yr}^{-1})$	1.5−3[9,10]	20[6]	11[7]	2−4[8]	4.2−6.8
r (pc)	0.2[11]	0.2[12]	0.2[7]	0.2[13]	0.3
n_{e}([S II]) (cm^{-3})	∼10 000[14,*]	500−1800[15]	≈1000[7]	≈500[13]	≈600
M_{ring}	0.06[16]	0.1[15]	0.5[7]	0.5−1.0[8]	1
$v\sin i(\,\mathrm{km\,s}^{-1})$	–	53	44	34	90
i (°)	43[17]	65[12]	60[18]	50[13]	60
$v_{\mathrm{exp}}(\,\mathrm{km\,s}^{-1})$	10[19]	30[15]	20[20]	19[13]	8
t_{kin} (10^4 yr)	2	0.7	1	1	3.7
$M_{\mathrm{kin}}/\dot M$	10−20	7	45	250	40−60
$\log(\mathrm{N/H})+12$	8.44[16]	8.91[6]	8.42[7]	7.51[13]	8.21

References: (1) Walborn et al. 1989; (2) Moffat 1983; (3) Walborn & Fitzpatrick 2000; (4) Taylor et al. 2014; (5) Arnett et al. 1989; (6) Hendry et al. 2008; (7) Nota et al. 1996; (8) Smith et al. 2013; (9) Blondin & Lundqvist 1993; (10) Martin & Arnett 1995; (11) Panagia et al. 1991; (12) Brandner et al. 1997a; (13) Smith et al. 2007; (14) Plait et al. 1995; (15) Brandner et al. 1997b; (16) Mattila et al. 2010; (17) Jakobsen et al. 1991; (18) O'Hara 2003; (19) Crotts & Heathcote 1991; (20) Hutsemekers et al. 1994.
Note: *Based on the fading of the [O III] λ5007 emission line.

Table 8. Peculiar transverse (in Galactic coordinates) and radial velocities, and the total space velocity of MN18 for two adopted proper motion measurements and three distances (see the text for details).

d (kpc)	$\mu_\alpha\cos\delta$ (mas yr^{-1})	μ_δ (mas yr^{-1})	v_l (km s^{-1})	v_b (km s^{-1})	v_{r} (km s^{-1})	v_* (km s^{-1})
4.4	−10.3±2.0[a]	−7.6±2.0[a]	−144.3±42.1	−12.6±41.9	9.6±1.3	145.2±42.0
4.4	−12.3±2.5[b]	−10.3±2.5[b]	−209.7±52.1	−39.5±52.1	9.6±1.3	213.6±52.0
5.6	−10.3±2.0[a]	−7.6±2.0[a]	−164.4±53.6	−18.2±53.4	22.1±1.3	166.9±53.1
5.6	−12.3±2.5[b]	−10.3±2.5[b]	−247.8±66.4	−52.4±66.4	22.1±1.3	254.2±66.2
7.1	−10.3±2.0[a]	−7.6±2.0[a]	−184.3±68.0	−25.3±67.6	20.3±1.3	187.1±67.6
7.1	−12.3±2.5[b]	−10.3±2.5[b]	−290.0±84.1	−68.7±84.1	20.3±1.3	298.7±83.9

Note: [a]SPM 4.0 (Girard et al. 2011); [b]UCAC4 (Zacharias et al. 2013).

to the stellar space velocity would affect the shape of the bipolar nebula, sweeping back the polar lobes, which is definitely not the case for the nebula around MN18. One cannot therefore exclude the possibility that the proper motion measurements for MN18 are erroneous (e.g. because of the presence of the equatorial ring) and that this star was actually born not far from its current position on the sky. There is some evidence in support of this possibility. Before discussing this evidence, we note that the small peculiar radial velocity of MN18 implies that the distance to this star did not change appreciably during its lifetime. Since the peculiar transverse velocity of MN18 is unrealistically high, and massive stars did not form in the interarm regions, we conclude that the most likely birthplace of MN18 is located in the Crux-Scutum Arm, i.e. at $d\sim4$ kpc.

In Section 5.1, we noted that the RSS slit crosses two other stars on both sides of MN18 (see also Fig. 13). The normalized spectrum of the brightest of these stars, located at RA(2000)=15$^{\mathrm h}$16$^{\mathrm m}$42$\overset{\mathrm s}{.}$97, Dec.(2000)=−58°22′19″.7 and indicated in Fig. 13 by a diamond, is shown in Fig. 14. In the following, we will use for this star its 2MASS name – 2MASS J15164297−5822197, or J1516−5822, in short. Like

in the case of MN18, the spectrum of J1516−5822 is dominated by absorption lines of H and He I. But additionally, it also shows weak absorption lines of He II at λλ4686, 5412 and 6527, which implies that J1516−5822 is of a spectral type earlier than B1 (Walborn & Fitzpatrick 1990), i.e. hotter than MN18. The Mg II λ4481 line is weak, which is typical of late O/B0 stars. The low quality of the blue part of the spectrum precludes us from using traditional classification criteria. Instead, we used the EW(Hγ)–absolute magnitude calibration by Balona & Crampton (1974), which for EW(Hγ)=3.14±0.20 Å implies that the spectral type of J1516−5822 is either O9 V, B0–1 III or B5–7 Ib. The B5–7 Ib classification could be rejected because of the presence of the He II lines in the spectrum. Thus, we tentatively classify J1516−5822 as a O9 V/B0–1 III star. EWs, FWHMs and RVs of main lines in the spectrum of J1516−5822 are summarized in Table 9.

Detection of a massive and therefore very rare star at only ≈17″ from MN18 suggests that both stars could be members of the same star cluster. Assuming that J1516−5822 is an O9 V star and using its 2MASS magnitudes (J,H,K$_{\mathrm s}$)=(11.35,10.85,10.63) (Cutri et al. 2003) and
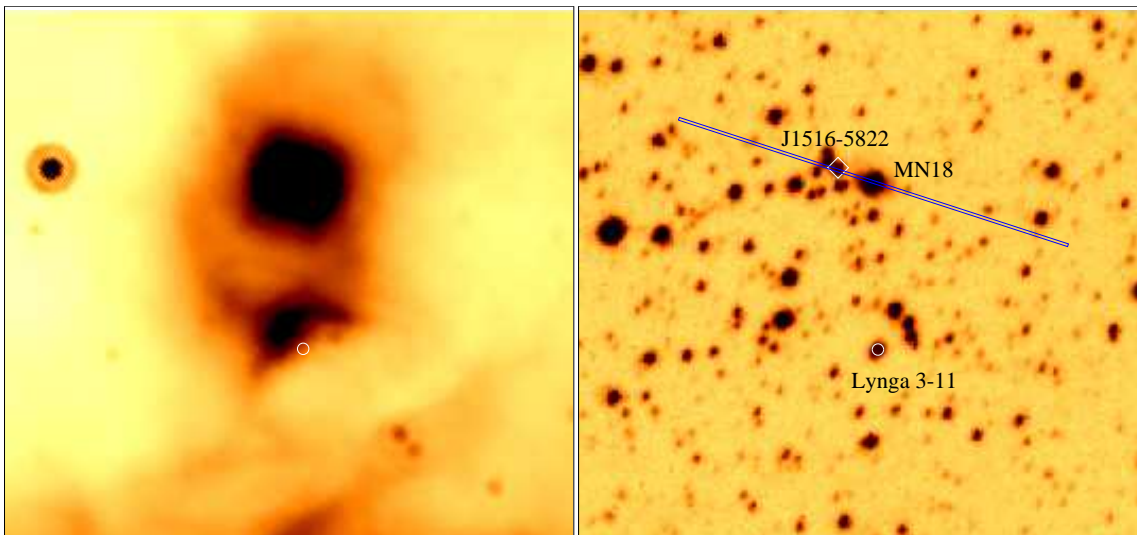
Figure 13. *Spitzer* MIPS 24 μm (left) and SHS Hα+[N II] images of a field around MN18 with positions of the newly-identified late O-/early B-type star 2MASS J15164297−5822197 and star 11 from Lynga (1964a) indicated by a diamond and circle, respectively. The orientation of the RSS slit (PA=72°) is shown by a (blue) rectangle. See text for details.

the photometric calibration of optical and infrared magnitudes for Galactic O stars by Martins & Plez (2006), we derived a K-band extinction towards J1516−5822 of $A_K = 0.59$ mag and a distance modulus of 13.36 mag, which corresponds to the distance of 4.7 kpc. The distance to J1516−5822 would be of $\approx$7 kpc if the spectral type of this star is B0–1 III. These estimates are consistent with the distance estimate of $5.6^{+1.5}_{-1.2}$ for MN18 (see Section 4.2), which supports the supposition that both stars might be members of the same cluster. Note that the mean RV of lines in the spectrum of J1516−5822 of 145 km s^{-1} is more than twice higher than v_{sys} of MN18. Although this difference might indicate that the two stars are unrelated to each other and are simply projected by chance along the same line-of-sight, it could also be understood if J1516−5822 is a close massive binary. Note also that the SPM 4.0 and UCAC4 proper motion measurements for this star ($\mu_\alpha \cos \delta = -28.42 \pm 2.89$, $\mu_\delta = 45.47 \pm 2.92$ and $\mu_\alpha \cos \delta = -36.0 \pm 3.5$, $\mu_\delta = 56.6 \pm 3.4$, respectively) differ significantly from those of MN18. These measurements, however, seem to be erroneous because they imply a huge space velocity of $\sim$1000–2000 km s^{-1} for any reasonable distance to the star. To conclude, the existing data did not allow us to prove or disprove the physical association between MN18 and J1516−5822.

Finally, we discuss the bright arc-like feature attached to the southwestern edge of the southeast lobe of the bipolar nebula around MN18 (see Section 2 and Figs 1 and 13). Fig. 13 shows that there is a star within the arc and near its apex. This star, located at RA(J2000)=15$^{\mathrm{h}}$16$^{\mathrm{m}}$40$^{\mathrm{s}}$76, Dec.(J2000)=−58°23′38″7, is listed in table V of Lynga (1964a) as a member of Lynga 3 under the number 11 (Lynga 3-11 hereafter). We speculate that the arc might be created because of interaction between the wind of Lynga 3-11 and the nebula (cf. Mauerhan et al. 2010; Burgemeister et al. 2013). The enhanced brightness of the arc at the place of possible contact with the nebula supports this pos-

Table 9. EWs, FWHMs and RVs of main lines in the spectrum of 2MASS J15164297−5822197.

λ_0(Å) Ion	EW(λ) (Å)	FWHM(λ) (Å)	RV (km s^{-1})
4340 Hγ	3.14±0.20	15.03±2.53	-96±16
4471 He I	1.00±0.04	9.58±0.40	-158±9
4922 He I	0.25±0.04	4.50±0.51	-163±8
5876 He I	0.87±0.04	6.73±0.27	-141±6
6563 Hα	1.74±0.05	10.62±0.24	-146±6
6678 He I	0.45±0.03	7.03±0.17	-150±6
7065 He I	0.71±0.03	11.16±0.29	-161±5

sibility. If the interaction indeed takes place, then Lynga 3-11 should be a source of strong wind, i.e. an OB star. In the absence of spectroscopic observations of Lynga 3-11, we estimate its spectral type using its 2MASS magnitudes (J,H,K$_s$)=(11.07,10.59,10.34) and a photometric calibration for Galactic O stars by Martins & Plez (2006), and assuming that this star is located at the same distance as MN18 (i.e. at $d = 5.6^{+1.5}_{-1.2}$ kpc). In doing so, we found that Lynga 3-11 should be of spectral type of O9.5 V (d=4.4 kpc), O6 V (d=5.6 kpc) or O4 V/O7.5 III (d=7.1 kpc). A spectroscopic study of this and other stars listed in Lynga (1964a) is necessary to check whether or not they form the parent cluster of MN18.

7 SUMMARY

In this Paper, we presented the results of optical spectroscopic observations of the blue supergiant MN18 and the equatorial ring of its hourglass-like nebula. MN18 was classified as B1 Ia and its spectrum was modelled using the radiative transfer code CMFGEN. We found the stellar effective temperature of 21.1±1.0 kK and the surface gravity of log g=2.75±0.20. Adopting an absolute visual magnitude of
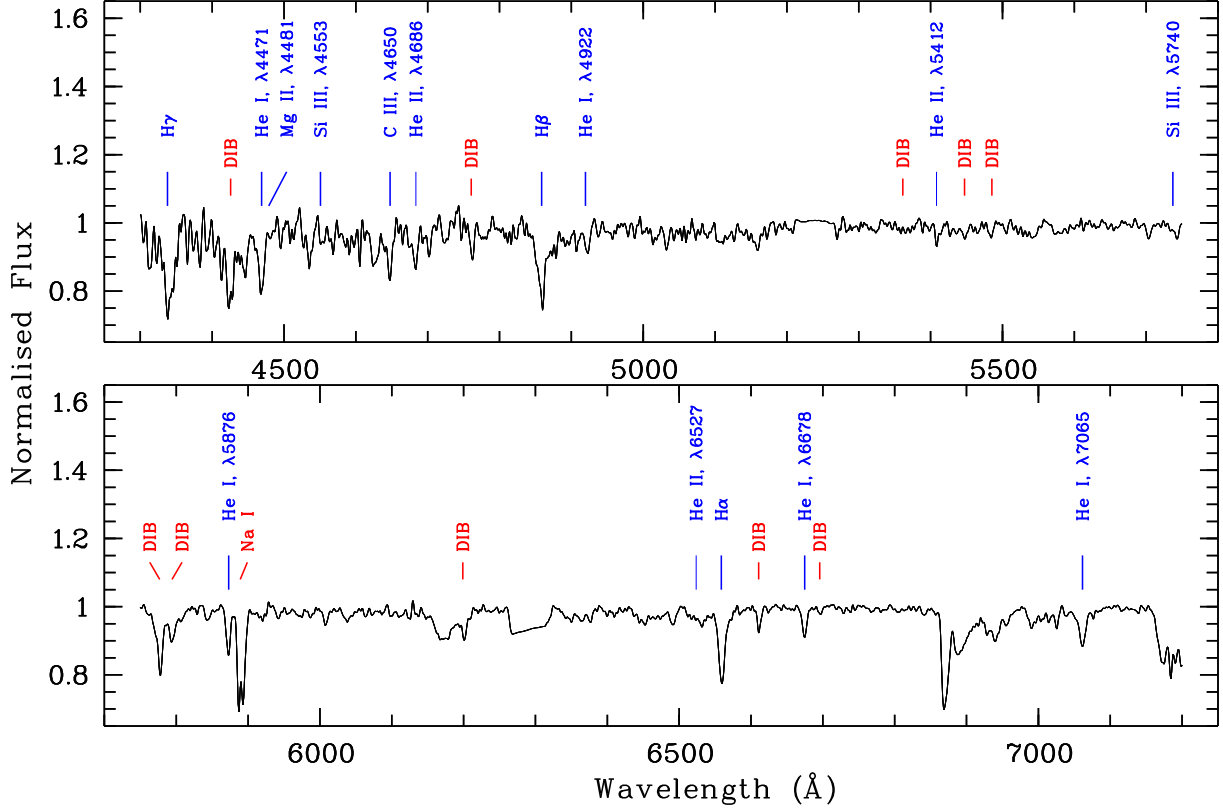
Figure 14. Normalized spectrum of 2MASS J15164297−5822197 obtained with the SALT on 2012 March 2 with the principal lines and most prominent DIBs indicated.

$M_V = -6.8 \pm 0.5$ (typical of B1 supergiants), MN18 has a luminosity of $\log L/L_\odot \approx 5.42 \pm 0.3$ and resides at a distance of $\approx 5.6^{+1.5}_{-1.2}$ kpc. It was shown that the nitrogen abundance of the stellar wind is enhanced by ≈ 4 times due to the CNO cycle and that the rotational velocity of MN18 is ≈ 100 km s^{-1}. The Hα line in the spectrum of MN18 changes from emission to absorption on a yearly time scale and shows a noticeable variability on a daily time scale. Correspondingly, the mass-loss rate estimates based on synthesizing the Hα line show a range of values from ≈ 2.8 to 4.5×10^{-7} M$_\odot$ yr^{-1}. Our photometric observations showed that the B, V and I_c magnitudes of MN18 changed by less than ≈ 0.1 mag during the last five years, while its $B - V$ and $B - I_c$ colours remained almost constant.

Analysis of the nebular spectrum revealed a factor of ≈ 2 overabundance of nitrogen, which implies that the equatorial ring is composed of processed material. The mass of the ring was found to be of ≈ 1 M$_\odot$, and its systemic and expansion velocities were estimated to be of -66.0 ± 1.3 km s^{-1} and 7.9 ± 1.2 km s^{-1}, respectively. The latter estimate implies the kinematic age of the equatorial ring of $\approx 3.7 \times 10^4$ yr.

The derived parameters of MN18 were compared with those predicted by stellar evolutionary models and a conclusion was drawn that this star is in the pre-red supergiant phase of its evolution. This conclusion agrees with previous suggestions that circumstellar nebulae around massive stars could be formed already near the end of the main sequence phase, and allowed us to suggest that the origin of the equatorial ring around MN18 is unlikely to be explained

within the framework of single star evolution. Based on the observed high percentage of binaries among massive stars and the possibility that massive stars did not born as rapid rotators, but became such because of mass transfer or mergers in binary systems, we suggested that these two binary interaction processes might be the main causes for the origin of nearly critically rotating stars and equatorial outflows from them.

The parameters of MN18 and its equatorial ring were also compared with those of four other blue supergiants with hourglass-like nebulae in the Milky Way (Sher 25, HD 168625, [SBW2007] 1) and the Large Magellanic Cloud (Sk−69°202). In particular, the comparison revealed that the luminosities of these stars span a wide range, from $\log(L/L_\odot) = 4.7$ to 5.8, which implies that the stellar luminosity is not a decisive factor in formation of equatorial rings. Also, the nitrogen abundances of the equatorial rings around MN18, HD 168625 and [SBW2007] 1 are consistent with the possibility that these rings were formed at the end of the main sequence stage or soon after it.

We found that MN18 is among a group of 25 stars suggested in the literature as being members of the star cluster Lynga 3. The reported age estimates for the cluster, however, about two orders of magnitude larger than the age of MN18, which raises doubts in their association. On the other hand, our spectroscopic observations led to a serendipitous discovery of a late O-/early B-type star at an angular separation of only ≈ 17 arcsec from MN18. The close proximity of the two massive and therefore very rare stars suggests

that both could be members of the same young star cluster. The distance estimates for these two stars support this suggestion. Moreover, we found an indication that another member of the putative cluster Lynga 3 is a massive star as well, which also points to the possibility that Lynga 3 is a young star cluster. Spectroscopic follow-ups of this and other stars around MN18 are necessary to prove whether Lynga 3 is the parent cluster to MN18.

8 ACKNOWLEDGEMENTS

REFERENCES

Anderson L. D., Zavagno A., Barlow M. J.,García-Lario P., Noriega-Crespo A., 2012, A&A, 537, A1
Arnett W. D., Bahcall J. N., Kirshner R. P., Woosley S. E. 1989, ARA&A, 27, 629
Asplund M., Grevesse N., Sauval A. J., Scott P., 2009, ARA&A, 47, 481
Balona L., Crampton D., 1974, MNRAS, 166, 203
Benjamin R. A. et al., 2003, PASP, 115, 953
Benvenuti P., D'Odorico S., Peimbert M., 1973, A&A, 28, 447
Berdnikov L. et al., 2012, Astron. Rep., 56, 290
Bestenlehner J. M. et al., 2011, A&A, 530, L14
Blondin J., Lundqvist, P., 1993, ApJ, 405, 337
Brandner W., Grebel E. K., Chu Y.-H., Weis K., 1997a, ApJ, 475, L45
Brandner W., Chu Y.-H., Eisenhauer F., Grebel E. K., Points S. D., 1997b, ApJ, 489, L153
Braun H., Langer N., 1995, A&A, 297, 483
Brott I. et al., 2011, A&A, 530, A115
Buckley D. A. H., Swart G. P., Meiring J. G., 2006, in Stepp L. M., ed., Proc. SPIE Conf. Ser. Vol. 6267, Ground-based and Airborne Telescopes. SPIE, Bellingham, p. 62670Z
Burgemeister S., Gvaramadze V., Stringfellow G.S., Kniazev A. Y., Todt H., Hamann W.-R., 2013, MNRAS, 429, 3305
Burgh E. B., Nordsieck K. H., Kobulnicky H. A., Williams T. B., O'Donoghue D., Smith M. P., Percival J. W., 2003, SPIE, 4841, 1463
Burrows C. J. et al., 1995, ApJ, 452, 680
Carey S. J. et al., 2009, PASP, 121, 76
Carraro G., Janes K. A., Costa E., Méndez R. A., 2006, MNRAS, 368, 1078
Chini R., Hoffmeister V. H., Nasseri A., Stahl O., Zinnecker H., 2012, MNRAS, 424, 1925
Chita S. M., Langer N., van Marle A. J., García-Segura G., Heger A., 2008, A&A, 488, L37
Chu Y.-H., Treffers R. R., Kwitter K. B., 1983, ApJS, 53, 937
Clark J. S., Larionov V. M., Arkharov A., 2005, A&A, 435, 239
Cohen M., Parker Q., Green A., Miszalski B., Frew D. J., Murphy T., 2011, MNRAS, 413, 514
Corradi R. L. M., Schwarz H. E., 1993, A&A, 268, 714
Crawford S. M. et al., 2010, in Silva D. R., Peck A. B., Soifer B. T., Proc. SPIE Conf. Ser. Vol. 7737, Observatory Operations: Strategies, Processes, and Systems III. SPIE, Bellingham, p. 773725
Crotts A. P. S., Heathcote S. R., 1991, Nature, 350, 683
Crowther P. A., Lennon D. J., Walborn N. R., 2006, A&A, 446, 279
Cutri R. M. et al., 2003, VizieR Online Data Catalog, 2246, 0
De Marco O., 2009, PASP, 121, 316
de Mink S. E., Langer N., Izzard R. G., Sana H., de Koter A., 2013, ApJ, 764, 166
de Mink S. E., Sana H., Langer N., Izzard R. G., Schneider F. R. N., 2014, ApJ, 782, 7
Dias W. S., Alessi B. S., Moitinho A., Lepine J. R. D., 2014, VizieR Online Data Catalog: Optically visible open clusters and Candidates (Dias+ 2002-2014)
Dopita M. A., 1973, A&A, 29, 387
Dopita M. A., Bell J. F., Chu Y.-H., Lozinskaya T. A., 1994, ApJS, 93, 455
Dufton P. L. et al., 2011, ApJ, 743, L22
Ekström S., Meynet G., Maeder A., Barblan F., 2008, A&A, 478, 467
Ekström S. et al., 2012, A&A, 537, A146
Esteban C., Vilchez J. M., Smith L. J., Clegg R. E. S., 1992, A&A, 259, 629
Fabian A. C., Hansen C. J., 1979, MNRAS, 187, 283
Fazio G. G. et al., 2004, ApJS, 154, 10
Frank A., Balick B., Davidson K., 1995, ApJ, 441, L77
Fransson C. et al., 2015, preprint (arXiv:1505.06669)
Frew D. J., Bojičić I. S., Parker Q. A., Pierce M. J., Gunawardhana M. L. P., Reid W. A., 2014, MNRAS, 440, 1080
Georgy C., Saio H., Meynet G., 2013, MNRAS, 439, L6
Gies D. R., 1987, ApJS, 64, 545
Girard T. M. et al., 2011, AJ, 142, 15
Glebbeek E., Gaburov E., Portegies Zwart S., Pols O. R., 2013, MNRAS, 434, 3497
Groh J. H., Meynet G., Ekström S., 2013, A&A, 550, L7
Groh J. H., Hillier D. J., Damineli A., Whitelock P. A., Marang F., Rossi C., 2009, ApJ, 698, 1698
Gröningsson P., Fransson C., Leibundgut B., Lundqvist P., Challis P., Chevalier R. A., Spyromilio J., 2008, A&A, 492, 481
Gvaramadze V. V., Menten K. M., 2012, A&A, 541, A7
Gvaramadze V. V. et al., 2009, MNRAS, 400, 524
Gvaramadze V. V., Kniazev A. Y., Hamann W.-R., Berd-

nikov L. N., Fabrika S., Valeev A. F., 2010a, MNRAS, 403, 760

Gvaramadze V. V., Kniazev A. Y., Fabrika S., Sholukhova O., Berdnikov L. N., Cherepashchuk A. M., Zharova A. V., 2010b, MNRAS, 405, 520

Gvaramadze V. V., Kniazev A. Y., Fabrika S., 2010c, MNRAS, 405, 1047 (Paper I)

Gvaramadze V. V., Pflamm-Altenburg J., Kroupa P., 2011, A&A, 525, A17

Gvaramadze V. V. et al., 2012a, MNRAS, 421, 3325

Gvaramadze V. V., Weidner C., Kroupa P., Pflamm-Altenburg J., 2012b, MNRAS, 424, 3037

Gvaramadze V. V., Miroshnichenko A. S., Castro N., Langer N., Zharikov S. V., 2014a, MNRAS, 437, 2761

Gvaramadze V. V., Kniazev A. Y., Berdnikov L. N., Langer N., Grebel E. K., Bestenlehner J. M., 2014b, MNRAS, 445, L84

Heger A., Langer N., 1998, A&A, 334, 210

Hendry M. A., Smartt S. J., Skillman E. D., Evans C. J., Trundle C., Lennon D. J., Crowther P. A., Hunter I., 2008, MNRAS, 388, 1127

Hillier D. J., Miller D. L., 1998, ApJ, 496, 407

Hillier D. J., Crowther P. A., Najarro F., Fullerton A. W., 1998, A&A, 340, 483

Hutsemekers D., van Drom E., Gosset E., Melnick J., 1994, A&A, 290, 906

Jakobsen P. et al., 1991, ApJ, 369, L63

Justham S., Podsiadlowski P., Vink J. S., 2014, ApJ, 796, 121

Kaufer A., Stahl O., Tubbesing S., Norregaard P., Avila G., Francois P., Pasquini L., Pizzella A., 1999, The Messenger, 95, 8

Kharchenko N. V., Piskunov A. E., Schilbach E., Röser S., Scholz R.-D., 2013, A&A, 558, A53

Kniazev A. Y., Pustilnik S. A., Grebel E. K., Lee H., Pramskij A. G., 2004, ApJS, 153, 429

Kniazev A. Y. et al., 2005, AJ, 130, 1558

Kniazev A. Y. et al., 2008, MNRAS, 388, 1667

Kniazev A. Y., Gvaramadze V. V., Berdnikov L. N., 2015, MNRAS, 449, L60

Kobulnicky H. A., Nordsieck K. H., Burgh E. B., Smith M. P., Percival J. W., Williams T. B., O'Donoghue D., 2003, in Iye M., Moorwood A. F. M., eds, Proc. SPIE Conf. Ser. Vol. 4841, Instrument Design and Performance for Optical/Infrared Ground-based Telescopes. SPIE, Bellingham, p. 1634

Kotak R., Vink J. S., 2006, A&A, 460, L5

Kwok S., Zhang Y., Koning N., Huang H.-H., Churchwell E., 2008, ApJS, 174, 426

Lamers H. J. G. L. M., Pauldrach A. W. A., 1991, A&A, 244, L5

Lamers H. J. G. L. M., Snow T. P., Lindholm D. M., 1995, ApJ, 455, 269

Lamers H. J. G. L. M., Nota A., Panagia N., Smith L. J., Langer N., 2001, ApJ, 551, 764

Langer N., 1997, in Nota A., Lamers H., eds, ASP Conf. Ser. Vol. 120, Luminous Blue Variables: Massive Stars in Transition. Astron. Soc. Pac., San Francisco, p. 83

Langer N., 1998, A&A 329, 551

Langer N., 2012, ARA&A, 50, 107

Langer N., Heger A., 1998, in Hubert A. M., Jaschek C., eds, Astrophysics and Space Science Library, Vol. 233, B[e]

Stars. Kluwer, Dordrecht, p. 235

Langer N., García-Segura G., Mac Low M.-M., 1999, ApJ, 520, L49

Langer N., Yoon S.-C., Petrovic J., Heger A., 2003, in Maeder A., Eenens P., eds, Proc. IAU Symp. 215, Stellar Rotation. Cambridge Univ. Press, Cambridge, p.535

Langer N., Cantiello M., Yoon S.-C., Hunter I., Brott I., Lennon D., Mink S., Verheijd M., 2008, in Bresolin F., Crowther P. A., Puls J., eds, Proc. IAU Symp. 250, Massive Stars as Cosmic Engines. Astron. Soc. Pac., San Francisco, p. 167

Livio M., Salzman J., Shaviv G., 1979, MNRAS, 188, 1

Lynga G., 1964a, Lund Medd. Astron. Obs. Ser. II, 139, 1

Lynga G., 1964b, Lund Medd. Astron. Obs. Ser. II, 140, 1

Maeder A., 1999, A&A, 347, 185

Maeder A., Desjacques V., 2001, A&A, 372, L9

Mackey J., Mohamed S., Gvaramadze V. V., Kotak R., Langer N., Meyer D. M.-A., Moriya T. J., Neilson H. R., 2014, Nature, 512, 282

Marston A. P., 1995, AJ, 109, 1839

Marston A. P., McCollum B., 2008, A&A, 477, 193

Martin C. L., Arnett D., 1995, ApJ, 447, 378

Martins F., Plez B., 2006, A&A, 457, 637

Martins F., Marcolino W., Hillier D. J., Donati J.-F., Bouret J.-C., 2015, A&A, 574, A142

Mason B. D., Hartkopf W. I., Gies D. R., Henry T. J., Helsel J. W., 2009, AJ, 137, 3358

Mastrodemos N., Morris M., 1999, ApJ, 523, 357

Mattila S., Lundqvist P., Gröningsson P., Meikle P., Stathakis R., Fransson C., Cannon R., 2010, ApJ, 717, 1140

Mauerhan J.C., Wachter S., Morris P.W., Van Dyk S.D., Hoard D.W., 2010, ApJ, 724, L78

Mermilliod J. C., 1995, in Egret D., Albrecht M., eds, Information and Online Data in Astronomy. Kluwer, Dordrecht, p. 127

Moffat A. F. J., 1983, A&A, 124, 273

Morel T., Marchenko S. V., Pati A. K., Kuppuswamy K., Carini M. T., Wood E., Zimmerman R., 2004, MNRAS, 351, 552

Morel T. et al., 2015, in Meynet G., Georgy C., Groh J., Stee P., eds., Proc. IAU Symp. 307, New windows on massive stars: asteroseismology, interferometry, and spectropolarimetry. Cambridge Univ. Press, Cambridge, p. 342

Morris M., 1981, ApJ, 249, 572

Morris T., Podsiadlowski P., 2009, MNRAS, 399, 515

Nota A., Livio M., Clampin M., Schulte-Ladbeck R., 1995, ApJ, 448, 788

Nota A., Pasquali A., Clampin M., Pollacco D., Scuderi S., Livio M., 1996, ApJ, 473, 946

O'Donoghue D. et al., 2006, MNRAS, 372, 151

O'Hara T. B., Meixner M., Speck A. K., Ueta T., Bobrowsky M. 2003, ApJ, 598, 1255

Owocki S. P., Gayley K. G., 1997, in Nota A., Lamers H., eds, ASP Conf. Ser. Vol. 120, Luminous Blue Variables: Massive Stars in Transition. Astron. Soc. Pac., San Francisco, p. 121

Packet W., 1981. A&A, 102, 17

Panagia N., Gilmozzi R., Macchetto F., Adorf H.-M., Kirshner R. P., 1991, ApJ, 380, L23

Parker Q. A. et al., 2005, MNRAS, 362, 689

Pauldrach A. W. A., Puls J.. 1990. A&A, 237. 409

Pelupessy I., Lamers H. J. G. L. M., Vink J. S., 2000, A&A,

359, 695

Petrov B., Vink J., Gräfener G., 2014, A&A, 565, A62

Petrovic J., Langer N., van der Hucht K. A., 2005, A&A, 435, 1013

Phillips J. P., Ramos-Larios G., 2008, MNRAS, 387, 407

Plait P., Lundqvist P., Chevalier R., Kirshner R., 1995, ApJ, 439, 730

Poe C. H., Friend D. B., Cassinelli J. P., 1989, ApJ, 337, 888

Reid M. J., Menten K. M., Zheng X. W., Brunthaler A., Xu Y., 2009, ApJ, 705, 1548

Rieke G. H. et al., 2004, ApJS, 154, 25

Russell S. C., Dopita M. A., 1992, ApJ, 384, 508

Sahai R. et al., 1999, AJ, 118, 468

Sana H., Evans C. J., 2011, in Neiner C., Wade G., Meynet G., Peters G., eds, Proc. IAU Symp. 272, Active OB Stars: Structure, Evolution, Mass Loss, and Critical Limits. Cambridge Univ. Press, Cambridge, p. 474

Sana H. et al., 2012, Science, 337, 444

Schönrich R., Binney J., Dehnen W., 2010, MNRAS, 403, 1829

Schmutz W., Hamann W.-R., Wessolowski U., 1989, A&A, 210, 236

Smartt S. J., Lennon D. J., Kudritzki R. P., Rosales F., Ryans R. S. I., Wright N., 2002, A&A, 391, 979

Smith N., 2007, AJ, 133, 1034

Smith N., Bally J., Walawender J., 2007, AJ, 134, 846

Smith N., Arnett W. D., Bally J., Ginsburg A., Filippenko A. V., 2013, MNRAS, 429, 1324

Smith N., Gehrz R. D., Campbell R., Kassis M., Le Mignant D., Kuluhiwa K., Filippenko A. V., 2011, MNRAS, 418, 1959

Sonneborn G. et al., 1998, ApJ, 492, L139

Spitzer Science Center, 2009, VizieR On-line Data Catalog, 2293, 0

Stahl O. et al., 2001, A&A, 375, 54

Steele I. A., Negueruela I., Clark J. S., 1999, A&AS, 137, 147

Stock D.J., Barlow M.J., Wesson R., 2011, MNRAS, 418, 2532

Stringfellow G. S., Gvaramadze V. V., Beletsky Y., Kniazev A. Y., 2012a, in Richards M. T., Hubeny I., eds, Proc. IAU Symp. 282, From Interacting Binaries to Exoplanets: Essential Modeling Tools. Cambridge Univ. Press, Cambridge, p. 267

Stringfellow G. S., Gvaramadze V. V., Beletsky Y., Kniazev A. Y., 2012b, in Drissen L., St-Louis N., Robert C., Moffat A. F. J., eds, ASP Conf. Ser. Vol. 465, Four Decades of Massive Star Research – A Scientific Meeting in Honor of Anthony J. Moffat. Astron. Soc. Pac., San Francisco, p. 514

Sugerman B. E. K., Lawrence S. S., Crotts A. P. S., Bouchet P., Heathcote S. R., 2002, ApJ, 572, 209

Suzuki T. K., Nakasato N., Baumgardt H., Ibukiyama A., Makino J., Ebisuzaki T., 2007, ApJ, 668, 435

Taylor W. D., Evans C. J., Simón-Díaz S., Sana H., Langer N., Smith N., Smartt S. J., 2014, MNRAS, 442, 1483

ud-Doula A., Owocki S. P., Townsend R. H. D., 2009, MNRAS, 392, 1022

Vallée J.P., 2014, AJ, 148, 5

Vink J. S., de Koter A., Lamers H. J. G. L. M., 1999, A&A, 350, 181

Vink J. S., Brott I., Gräfener G., Langer N., de Koter A., Lennon D.J., 2010, A&A, 512, L7

Wade G. A. et al., 2014, in Petit P., Jardine M., Spruit H. C., eds., Proc. IAU Symp. 302, Magnetic Fields throughout Stellar Evolution. Cambridge Univ. Press, Cambridge, p. 265

Walborn N. R., Fitzpatrick E. L., 1990, PASP, 102, 379

Walborn N. R., Fitzpatrick E. L., 2000, PASP, 112, 50

Walborn N. R., Prevot M. L., Prevot L., Wamsteker W., Gonzalez R., Gilmozzi R., Fitzpatrick E. L., 1989, A&A, 219, 229

Wickramasinghe D. T., Tout C. A., Ferrario L., 2014, MNRAS, 437, 675

Zacharias N., Finch C.T., Girard T.M., Henden A., Bartlett J.L., Monet D.G., Zacharias M.I., 2013, AJ, 145, 44

Zasov A. V., Kniazev A. Y., Pustilnik S. A., Pramsky A. G., Burenkov A. N., Ugryumov A. V., Martin J.-M., 2000, A&AS, 144, 429